Article

Metastable hexagonal close-packed palladium hydride in liquid cell TEM

https://doi.org/10.1038/s41586-021-04391-5

Received: 6 November 2020

Accepted: 23 December 2021

Published online: 23 March 2022

Check for updates

Jaeyoung Hong[1,17], Jee-Hwan Bae[1,17], Hyesung Jo[2], Hee-Young Park[3], Sehyun Lee[3], Sung Jun Hong[4,5], Hoje Chun[5], Min Kyung Cho[1], Juyoung Kim[1], Joodeok Kim[6,7], Yongju Son[6,7], Haneul Jin[3], Jin-Yoo Suh[8], Sung-Chul Kim[1], Ha-Kyung Roh[9], Kyu Hyoung Lee[10], Hyung-Seok Kim[9], Kyung Yoon Chung[9,11], Chang Won Yoon[3,11,12], Kiryeong Lee[1], Seo Hee Kim[1], Jae-Pyoung Ahn[1], Hionsuck Baik[13], Gyeung Ho Kim[1], Byungchan Han[5], Sungho Jin[14], Taeghwan Hyeon[6,7], Jungwon Park[6,7,15], Chang Yun Son[16]✉, Yongsoo Yang[2]✉, Young-Su Lee[8]✉, Sung Jong Yoo[3,11,12]✉ & Dong Won Chun[1,8]✉

Metastable phases—kinetically favoured structures—are ubiquitous in nature[1,2]. Rather than forming thermodynamically stable ground-state structures, crystals grown from high-energy precursors often initially adopt metastable structures depending on the initial conditions, such as temperature, pressure or crystal size[1,3,4]. As the crystals grow further, they typically undergo a series of transformations from metastable phases to lower-energy and ultimately energetically stable phases[1,3,4]. Metastable phases sometimes exhibit superior physicochemical properties and, hence, the discovery and synthesis of new metastable phases are promising avenues for innovations in materials science[1,5]. However, the search for metastable materials has mainly been heuristic, performed on the basis of experiences, intuition or even speculative predictions, namely 'rules of thumb'. This limitation necessitates the advent of a new paradigm to discover new metastable phases based on rational design. Such a design rule is embodied in the discovery of a metastable hexagonal close-packed (hcp) palladium hydride (PdH_x) synthesized in a liquid cell transmission electron microscope. The metastable hcp structure is stabilized through a unique interplay between the precursor concentrations in the solution: a sufficient supply of hydrogen (H) favours the hcp structure on the subnanometre scale, and an insufficient supply of Pd inhibits further growth and subsequent transition towards the thermodynamically stable face-centred cubic structure. These findings provide thermodynamic insights into metastability engineering strategies that can be deployed to discover new metastable phases.

The advent of liquid cell transmission electron microscopy (TEM) enables the direct imaging and growth of materials in liquids. The electron beam generated inside the microscope transfers high energy to the irradiated suspending liquid; water molecules decompose into radicals and molecules, including hydrated electrons (e_h^-), hydroxyl radicals ($OH^•$), hydrogen radicals ($H^•$) and hydrogen molecules (H_2). This radiation chemistry of water results in distinct phenomena in liquid cell TEM. Examples include nanocrystal growth by the reaction of precursors and e_h^-, the most reactive radiolysis product, and bubbles formed by a high H_2 concentration.

Face-centred cubic (fcc) palladium hydride (PdH_x) constitutes the most important model system for fundamental studies of H in metals[6,7]. In general, the PdH_x phase can form on the adsorption and dissociation of H_2 on the Pd surface, followed by surface, subsurface and interstitial site occupations of hydrogen atoms[6]. Similar to metallic Pd, the PdH_x phase has a fcc structure in which the octahedral interstitial sites are occupied by H atoms, providing two distinct phases: a low-H-content α-phase and a high-H-content β-phase ($x \leq 0.7$)[6].

In this study, we synthesized metastable hexagonal close-packed (hcp) PdH_x nanoparticles by liquid cell TEM using a graphene liquid cell

[1]Advanced Analysis Center, Korea Institute of Science and Technology, Seoul, Korea. [2]Department of Physics, Korea Advanced Institute of Science and Technology, Daejeon, Korea. [3]Center for Hydrogen Fuel Cell Research, Korea Institute of Science and Technology, Seoul, Korea. [4]Integrated Science and Engineering Division, UIC, Yonsei University, Seoul, Korea. [5]Chemical and Biomolecular Engineering Department, Yonsei University, Seoul, Korea. [6]Center for Nanoparticle Research, Institute for Basic Science (IBS), Seoul, Korea. [7]School of Chemical and Biological Engineering and Institute of Chemical Processes, Seoul National University, Seoul, Korea. [8]Center for Energy Materials Research, Korea Institute of Science and Technology, Seoul, Korea. [9]Center for Energy Storage Research, Korea Institute of Science and Technology, Seoul, Korea. [10]Department of Materials Science and Engineering, Yonsei University, Seoul, Korea. [11]Division of Energy & Environment Technology, KIST School, Korea University of Science and Technology, Seoul, Korea. [12]KHU-KIST Department of Converging Science and Technology, Kyung Hee University, Seoul, Korea. [13]Korea Basic Science Institute, Seoul, Korea. [14]Materials Science and Engineering Program, Department of Mechanical and Aerospace Engineering, University of California San Diego, La Jolla, CA, USA. [15]Institute of Engineering Research, Seoul National University, Seoul, Korea. [16]Department of Chemistry and Division of Advanced Materials Science, Pohang University of Science and Technology, Pohang, Korea. [17]These authors contributed equally: Jaeyoung Hong, Jee-Hwan Bae. ✉e-mail: changyunson@postech.ac.kr; yongsoo.yang@kaist.ac.kr; lee0su@kist.re.kr; ysj@kist.re.kr; chundream98@kist.re.kr

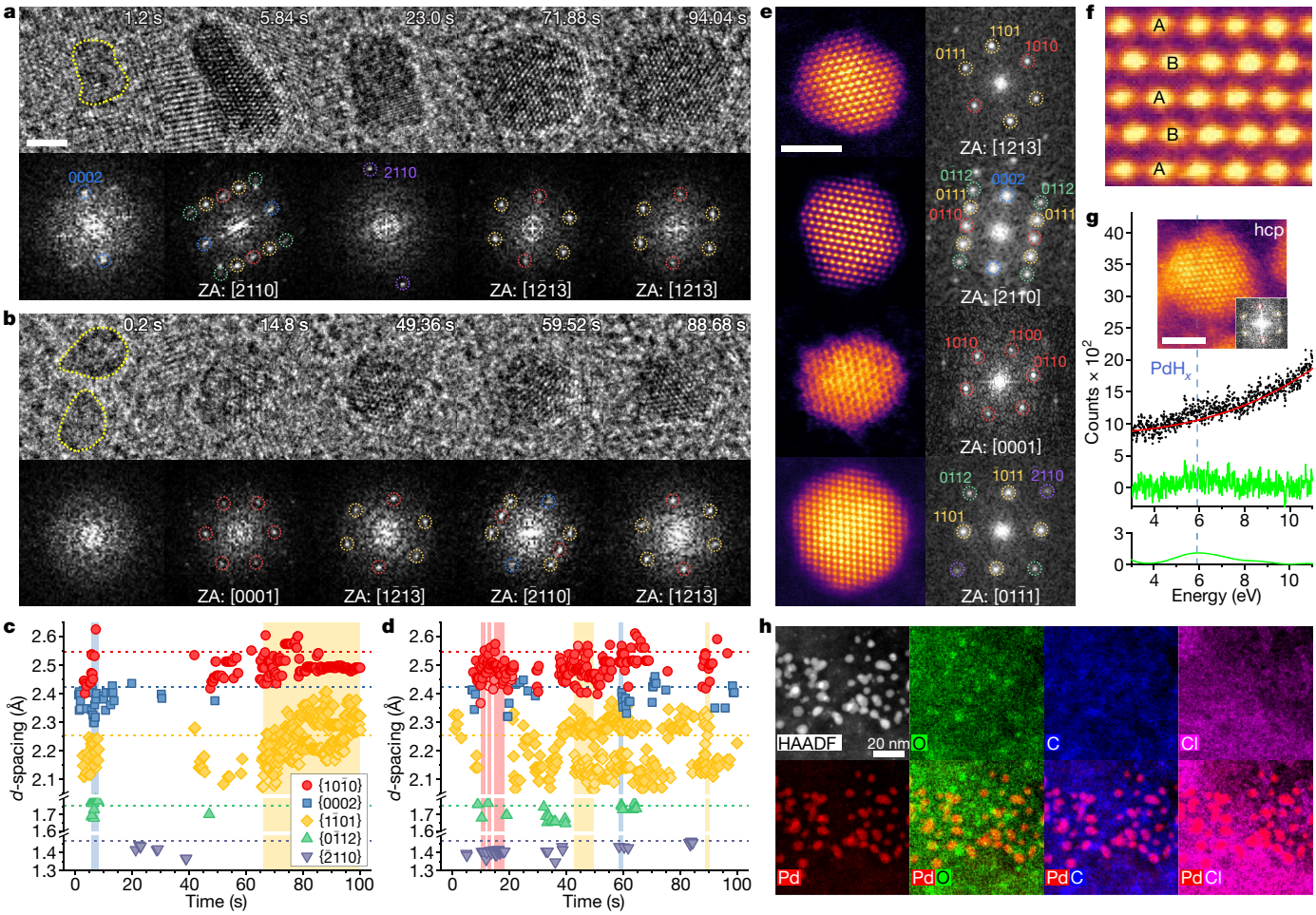

Fig. 1 | In situ and ex situ TEM analysis of hcp Pd nanoparticles in a GLC. **a**, **b**, Snapshots from Supplementary Video 1 and 2 of Pd nanoparticle growth and corresponding fast Fourier transforms (FFTs), with the growth occurring through monomer attachment (particle 1) (**a**) and coalescence (particle 2) (**b**) under an EDR of around 1.0×10^4 $e^- Å^{-2} s^{-1}$ (high EDR). Every zone axis (ZA) pattern matched that of the hcp lattice. Notably, hcp particles form regardless of lattice fringes from a two-dimensional NaCl crystal (Supplementary Video 3). **c**, **d**, Temporal changes in the interplanar distance of five low-index planes in particles 1 (**c**) and 2 (**d**). Blue-, yellow- and red-shaded boxes in **c** and **d** represent time spans when the particle was aligned along the [$\bar{2}$110], [1$\bar{2}$1$\bar{3}$] and [0001] zone axes of hcp, respectively. Horizontal dashed lines represent the mean *d*-spacings of each crystallographic plane obtained from ex situ measurements. **e**, Ex situ HR-STEM images and FFTs of four different particles formed under an EDR of 675 $e^- Å^{-2} s^{-1}$ (medium EDR), which were found to be consistent with the [1$\bar{2}$1$\bar{3}$], [$\bar{2}$110], [0001] and [01$\bar{1}$1] zone axis patterns of the hcp lattice. Dashed circles represent low-index planes coloured according to each family of planes. **f**, ABAB stacking of Pd atoms observed in the particle along the [$\bar{2}$110] zone axis in **e**. **g**, Original and denoised EEL spectra obtained from a hcp nanoparticle (inset) aligned at the [1$\bar{2}$1$\bar{3}$] zone axis. Black dots are raw data, the red line is the fitted background and the green line shows the background-removed EEL spectrum. The smooth green line in the bottom box shows the denoised signal. **h**, EDS map of the nanoparticles indicating that they consist of only one element, Pd. All the images were acquired ex situ except the snapshot images in **a** and **b**. Scale bars, 2 nm unless stated otherwise.

(GLC)[8]. Specifically, a Pd precursor solution was encapsulated between two multilayer graphene layers, and e_h^- produced by the electron beam initiated the nucleation and growth of nanoparticles[9] (Supplementary Videos 1, 2), as observed by TEM (Methods). Owing to the free rotation of the nanoparticles in the liquid[10], diffraction patterns (DPs) with distinct zone axes can be acquired to determine their crystal structures.

Notably, the DPs obtained from in situ TEM (Fig. 1a, b) and ex situ high-resolution scanning transmission electron microscopy (HR-STEM) (Fig. 1e, Methods) images of the synthesized nanoparticles corresponded to a hcp lattice rather than a fcc lattice, the structure of almost every Pd compound ever reported[11,12], regardless of growth pathway, that is, monomer attachment (particle 1, Fig. 1a, c) or coalescence (particle 2, Fig. 1b, d). In particular, no phase transformation from fcc to hcp was observed: the particles with hcp structures were hcp from the beginning. The interplanar distance values of low-index planes remained almost unchanged during growth, showing the stability of the structure (Fig. 1c, d). ABAB stacking, a distinctive characteristic of hcp phases, was clearly revealed in the HR-STEM image (Fig. 1f).

The statistical analysis of lattice constants derived from the DPs (Methods) showed that the volume per formula unit or per Pd atom ($V_{f.u.}$) of the hcp nanoparticles increased by approximately 23% with respect to the $V_{f.u.}$ of the ideal hcp Pd obtained from density functional theory (DFT) calculations (Fig. 1c, d and Extended Data Fig. 1a), indicating that the produced nanoparticles were more likely to be a Pd compound than pure Pd. Furthermore, the presence of an electron energy loss spectroscopy (EELS) spectrum peak at around 5.9 eV, a distinctive characteristic of fcc PdH_x (ref. [6]), together with the exclusive presence of a Pd peak in the energy dispersive X-ray spectroscopy (EDS) spectrum, indicates the formation of PdH_x (Fig. 1g, h and Extended Data Fig. 1b–d; Methods).

The stabilities of PdH_x ($0 \le x \le 1$) in fcc and hcp structures were examined by DFT calculations and Monte Carlo (MC) simulations using the embedded atom method (EAM) potential model[13] (Methods). As expected, the total energy of the bulk periodic PdH_x crystals estimated from both DFT and MC calculations predicted that the fcc structure was more stable than the hcp structure for all values of x, with the H atoms in PdH_x preferring to occupy the octahedral interstitial sites regardless

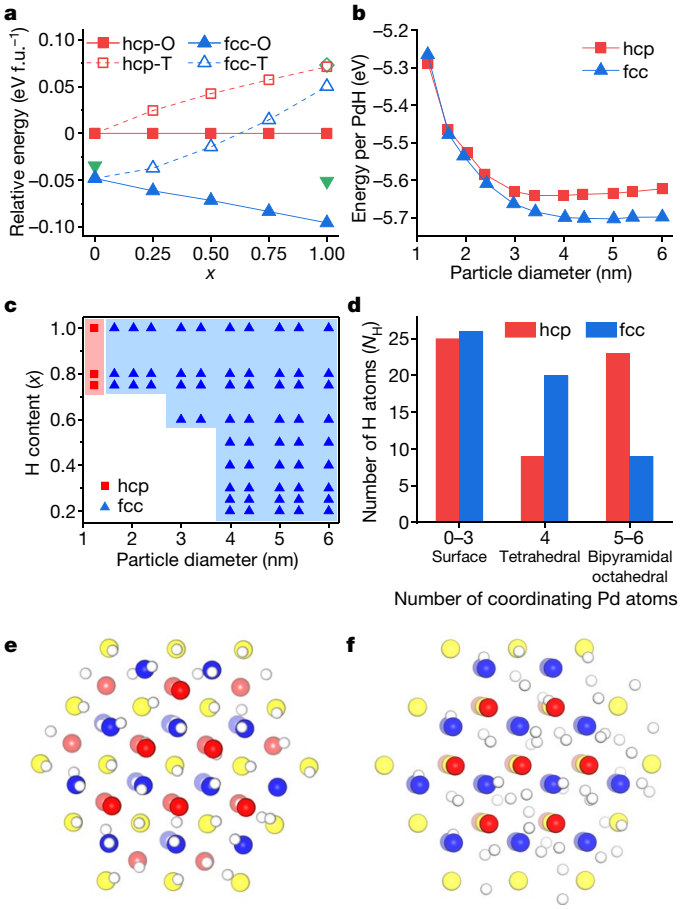

Fig. 2 | Thermodynamic stability of fcc/hcp PdH_x nanoparticles predicted by simulations. a, Comparison of total energy per formula unit (f.u.) for various PdH_x bulk crystals. Energies calculated with EAM potentials are represented as blue triangles (fcc) and red squares (hcp). Solid lines/filled symbols and dashed lines/empty symbols represent octahedral (O) and tetrahedral (T) positional occupation of H, respectively, with the energy of hcp-O for reference. The green-filled inverse triangles and green-outlined empty diamond represent the energy difference between fcc-O/hcp-O and hcp-T/hcp-O, respectively, including the zero-point vibrational energy obtained from DFT calculations. **b**, MC-simulated thermodynamic stability of equivalenced PdH nanoparticles with different particle sizes and crystal packing. Pd atoms are fixed at DFT-optimized positions with either fcc or hcp structures, whereas H atoms are allowed to move freely until the energy and structure are equilibrated under ambient conditions. **c**, Phase diagram of finite-sized PdH_x nanoparticles with different diameters and H contents. The uncategorized area for small nanoparticles with low H contents represents the region where fcc and hcp structures show very similar energies. **d**–**f**, Partitioning of H atoms (**d**) (white spheres in **e** and **f**) and snapshots of equilibrated structures obtained from MC simulations for subnanometre (12 Å) PdH nanoparticles (**e**, **f**). The positions of Pd atoms (large spheres with colours representing different layers) are fixed in the fcc (**e**) and hcp (**f**) crystal lattices. Each nanoparticle contains five Pd layers with ABCA′B′ (**e**) and ABA′B′A″ (**f**) packing. Owing to the small number of layers, nearly half of the H atoms are located in the surface region (with number of coordinating Pd atoms of 0–3) and extra stabilization by the 1–4 AA′ overlap is lost in many fcc-O sites, thus reducing the stability of fcc-O sites in this small nanoparticle. By contrast with the bulk crystal, more internal H atoms in the fcc nanoparticle occupy T sites than O sites.

of the crystal packing (Fig. 2a). Therefore, the simulation results on the ideal bulk PdH_x do not support the formation of hcp nanoparticles.

Surprisingly, however, MC simulations with various particle sizes revealed that hcp PdH is more stable than fcc PdH for nanocrystals with diameters of less than 2 nm (Fig. 2b, c). The occupancy of H atoms depends largely on the size as well as the crystal packing (Extended Data Fig. 2); the large fraction of surface Pd atoms with incomplete secondary coordination results in irregular size dependencies. Consequently, the extra stabilization of O sites introduced by the overlap of layers 1 and 4 (ABCA′) in fcc Pd is significantly reduced for the small particles that accommodate only five layers of Pd atoms (Fig. 2e and Extended Data Fig. 2g). By contrast, the stability of O sites in the hcp Pd nanoparticle would not be affected by the presence of a small number of layers, as no Pd atoms vertically overlap with the O sites in hcp stacking (Fig. 2f and Extended Data Fig. 2h). Interestingly, hcp structures are preferred at higher H contents ($x > 0.6$, Fig. 2c), mainly because of the difference in the surface H atom fraction between high ($x = 1$, Extended Data Fig. 2a) and low ($x = 0.2$, Extended Data Fig. 2d) H contents, which implies that a continuous supply of H radicals in the liquid cell could facilitate the formation of hcp PdH_x.

To verify the MC-derived formation mechanism of hcp PdH_x, we tested the synthesis of PdH_x nanoparticles under different growth conditions by (1) modulating the H concentration by tuning the electron dose rate (EDR) to three different values of 9,934 (high), 675 (medium) and 39 (low) $e^- Å^{-2} s^{-1}$ (Methods), (2) controlling the concentration of the Pd precursor (3.67, 10, 18, 36.7 and 73 mM) and (3) adopting a different synthesis environment based on a Si_3N_4 liquid cell (SLC) with static (non-flow) and flow modes (Fig. 3). These experiments demonstrate three distinctive trends.

First, conditions with higher H and lower Pd in the solution facilitate the formation of hcp nanoparticles. For example, a higher EDR and lower Pd concentration result in the dominance of the hcp phase (Fig. 3 and Extended Data Fig. 3a, b). On the other hand, a lower EDR and a higher Pd concentration, as well as bubble formation (Extended Data Fig. 4a, b), promote the formation of fcc nanoparticles.

Second, even though the $V_{f.u.}$ values of the hcp PdH_x nanoparticles show a broad distribution, larger $V_{f.u.}$ values were observed at higher EDRs and lower Pd concentrations (Fig. 3). At a fixed Pd concentration, we could see clearly lower $V_{f.u.}$ values in the particles obtained with low EDRs compared to those from higher EDRs. The H content x in hcp PdH_x was estimated by comparing the $V_{f.u.}$ measured in the experiment with that from the DFT calculations (Extended Data Fig. 5a). The approximate H content x grows as the EDR increases and approaches unity at high EDR. We expect a rapid increase in equilibrium hydrogen pressure (on a logarithmic scale) even with a small increase in x, as in the hydrogen-rich β-phase of fcc PdH_x (around 0.6 and higher)[7]. Here the H* or H_2 concentration in the solution (Extended Data Fig. 3a, b) corresponds to the equilibrium hydrogen pressure. This explains the relatively small difference between the $V_{f.u.}$ values of the high and medium EDRs (Fig. 3 and Extended Data Fig. 5); the hydrogen pressure increase from the medium to the high EDR can induce only a small increase in x, that is, $V_{f.u.}$. When x decreases, the same degree of logarithmic pressure change can cause a larger variation in x, which is reflected in a larger difference between the $V_{f.u.}$ values of the medium and low EDRs.

Third, nanoparticles synthesized in the SLC also exhibit a hcp structure in both static and flow modes (Methods). This result indicates that the special environment provided in the GLC, such as the pressure build-up because of van der Waals forces[14,15] or the hexagonal carbon array of graphene, which can serve as a template for the epitaxial growth of PdH_x (ref. [16]), can be excluded from the main mechanism of hcp PdH_x formation.

Notably, in the SLC experiments, the proportion of hcp particles exhibits a sharp decrease when the EDR is reduced, which is more prominent than the decrease observed in the GLC. In addition, the $V_{f.u.}$ values of the hcp PdH_x nanoparticles formed in the SLC were smaller than those of the hcp nanoparticles in the GLC under the same EDR (Extended Data Fig. 5a). The distinction between the GLC and SLC could be attributed to the enhanced Pd diffusion in the SLC[17], in which Pd precursor molecules are constantly supplied to the e-beam irradiated area as a consequence of the larger liquid volume encapsulated inside

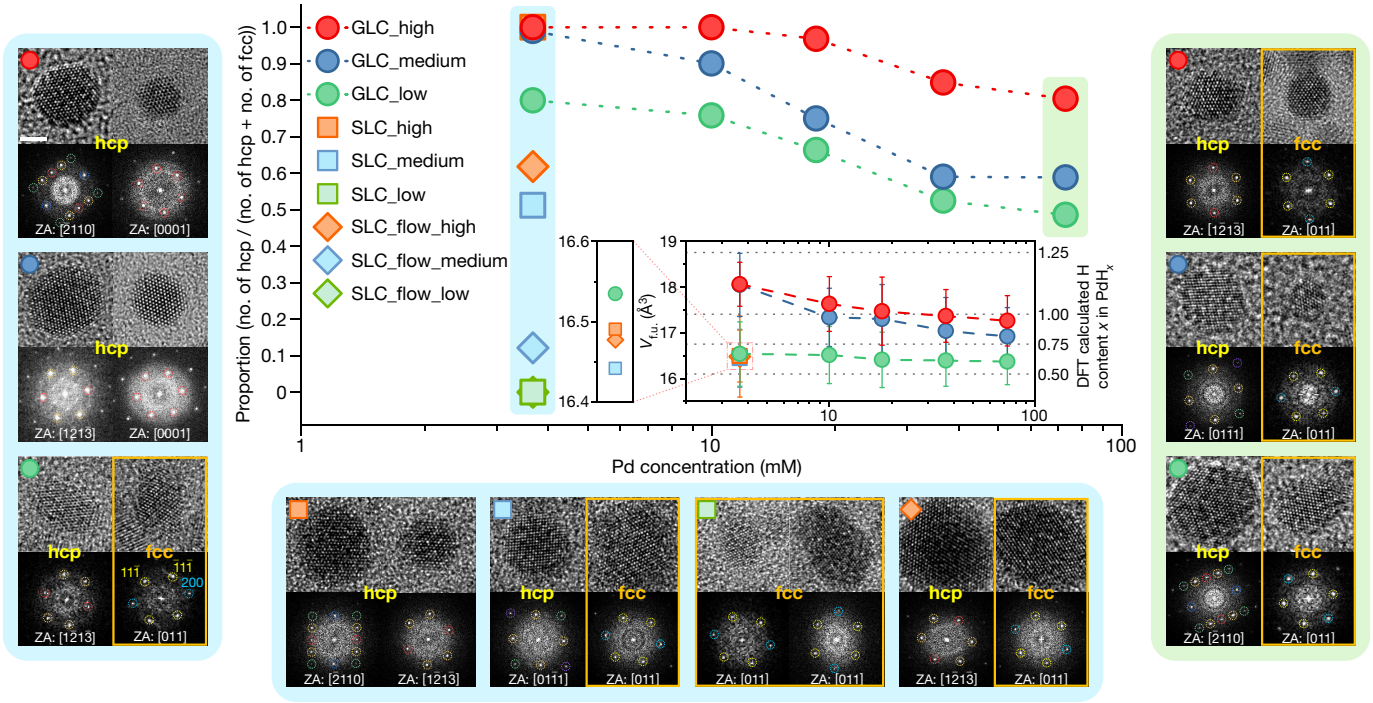

Fig. 3 | Dependence of nanoparticle structure on EDR, Pd solution concentration and liquid cell type. Proportion of hcp particles formed under electron beam irradiation under several different conditions. Red, blue and green represent high, medium and low EDR conditions, respectively, whereas circle, square and diamond shapes denote the liquid system of the GLC, SLC and SLC with liquid flow, respectively. The inset shows the change in $V_{f.u.}$ of hcp particles in each condition, with error bars representing standard deviations and a magnified plot of the region where four points overlap. Grey horizontal dotted lines in the inset show the H content of hcp PdH_x derived from DFT calculations. The numbers of particles used for $V_{f.u.}$ analysis for each condition are shown in Extended Data Fig. 5c. Three groups of HR-TEM images and the corresponding FFTs that encircle the main plot show representative particles formed under several selected conditions. The blue-shaded group shows particles formed in 3.67 mM Pd solution, with images in the left column showing GLC cases under high, medium and low EDRs and images in the bottom row showing SLC cases under three EDRs and with liquid flow under high EDR. The green-shaded group shows particles formed from 73 mM Pd solution in the GLC under three EDRs. Symbols denoting each case appear in the top left of each set of particles. All the images were acquired ex situ, except for the set of particles formed in the GLC under high EDR, which were taken in situ. Scale bar, 2 nm. ZA, zone axis.

the liquid cell. By contrast, the encapsulated volume in the GLC is much smaller[18]; hence, only a limited amount of Pd can diffuse into the irradiated area, creating a lower effective Pd concentration, which favours the formation of the hcp phase. In addition, an enhanced dynamic motion of the nanoparticles, possibly induced by window charging in the SLC, might increase the probability of particles entering unirradiated areas during growth and thereby being exposed to a lower H environment[19]. Furthermore, the differences observed in the GLC and SLC become more conspicuous when the liquid solution is flowed into the SLC. The configuration of the e-beam irradiation in a fixed area with liquid flow during particle growth could develop lower solution concentrations of radiolysis products, including e_h^-, H• and H_2, which results in a reduced proportion of hcp structures and a lower $V_{f.u.}$ at a fixed EDR. Nanoparticle size and distribution were investigated as well, but there was no clear trend with respect to EDR or Pd concentration in either the GLC or SLC, possibly because of the complex environment in TEM liquid cells (Extended Data Fig. 6).

All the data indicate that the interplay of H and Pd concentrations is key in the formation of hcp structures, as predicted by MC simulations; higher H and lower Pd concentrations facilitate the formation of particles in the hcp phase.

To further verify the effect of a change in EDR, we used a newly designed system for electron-beam-induced synthesis outside a TEM (Extended Data Fig. 4c–e, Methods). All the particles produced in the new system exhibited a fcc structure with lattice constants slightly larger than those of the standard fcc Pd (Extended Data Fig. 4d), with an x value of only approximately 0.002. This can be attributed to a lower H supply owing to the far lower EDR, indicating that the hcp PdH_x formation process depends strongly on the anomalous H supply originating from radiolysis.

An abundant supply of H may also modulate the growth kinetics. According to the DFT calculations, the addition of another layer of Pd to the (111) surface of fcc PdH requires more energy than addition of a layer to the (0001) surface of hcp PdH. This higher energy cost is compensated by a more exothermic reaction with H atoms in the fcc structure (Extended Data Fig. 7). This result can be interpreted as the passivation of fcc PdH particles by H radicals, which in turn stabilizes the surface and disfavours the further incorporation of Pd, resulting in slower growth. In addition, the more rapid growth of hcp particles would quickly deplete the Pd precursors, further suppressing the growth of fcc particles.

As a metastable solid phase initially forms, it dissolves and is replaced by a more stable phase through several thermodynamically permissible pathways until the most stable phase is formed, as described by Ostwald[3]. Hence, one remaining question is how a hcp nanoparticle maintains its crystal structure rather than transforming into a fcc structure, even when it grows into a size regime that is unstable for hcp structures (Fig. 2c and Extended Data Fig. 6a, c, f–k). In general, the synthesis of a nanocrystal in an aqueous solution requires a sufficient supply of precursors to facilitate the formation of a thermodynamically stable phase. By contrast, in liquid cell TEM, the metastable phases initially grown on irradiation form in a region of supersaturated precursors with

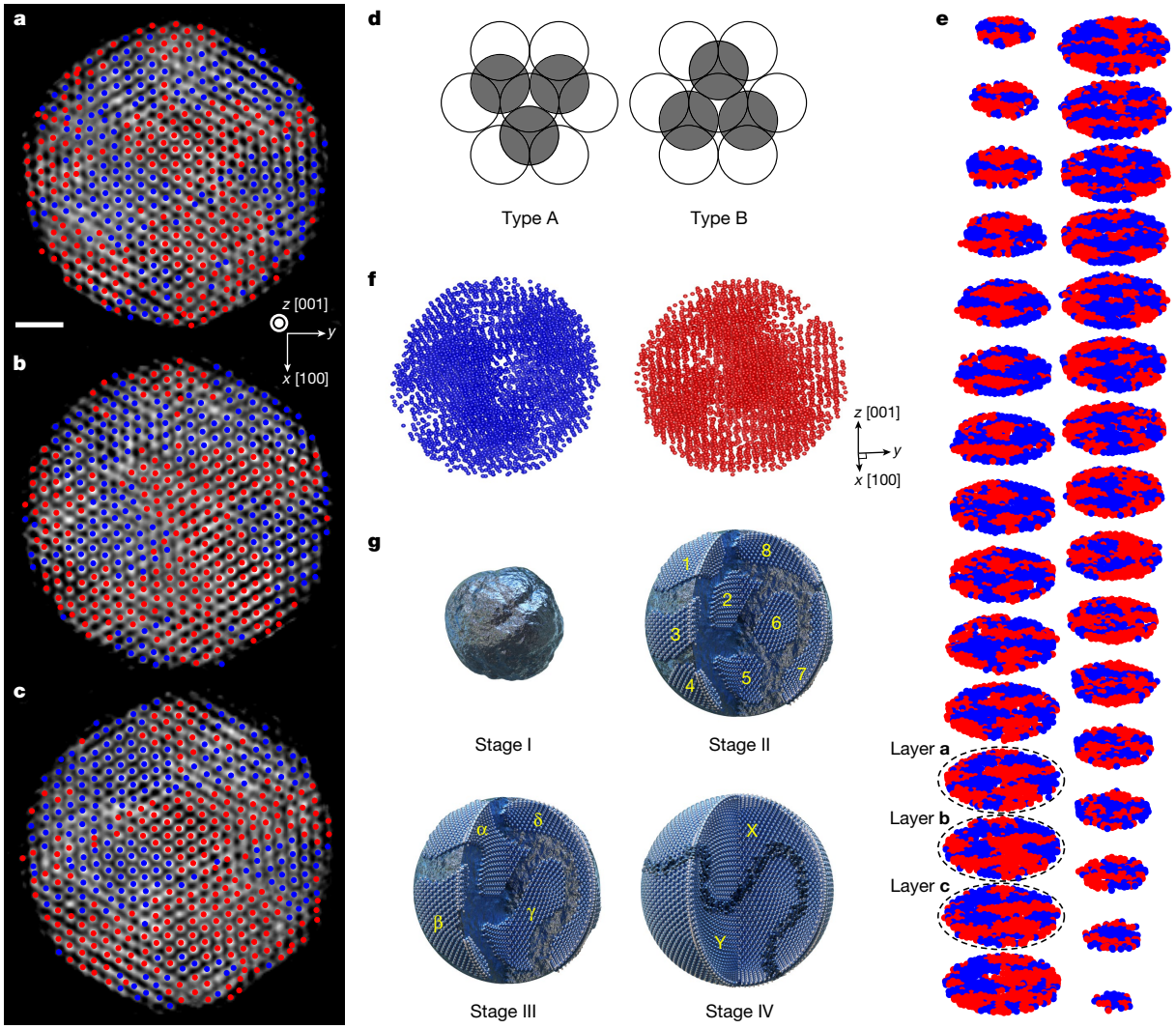

Fig. 4 | 3D single-atom-level structural analysis of a PdH_x nanoparticle. a–c, Reconstruction intensity and traced atomic coordinates of three consecutive atomic layers of a nanoparticle formed under a medium EDR in the GLC. The greyscale background represents the sliced intensity of the reconstructed 3D tomogram, and blue and red dots represent the positions of traced atoms belonging to ABAB and BABA stacking, respectively. Interlayer atoms (which do not clearly belong to one of the hcp atomic layers) are plotted in the layers that best represent their in-plane positions. Scale bar, 1 nm. **d**, Schematic diagram of the two different types (types A and B) of nearest-neighbour arrangements in a hcp crystal. **e**, Hexagonal stacking types revealed by 3D atomic structural analysis via AET. Each slice represents an atomic layer of the nanoparticle perpendicular to the hexagonal *c* axis, where ABAB-type and BABA-type regions are coloured blue and red, respectively. Layers corresponding to those in **a**–**c** are marked with black dashed lines. **f**, 3D atomic structures separately drawn for atoms of each stacking type. ABAB-type and BABA-type atoms are blue and red, respectively. **g**, Scheme of particle formation by multistep crystallization. Stage I: the Pd precursors assemble into an amorphous cluster. Stage II: crystalline nuclei (1–8) form at multiple sites within the amorphous cluster. Stage III: nuclei grow by a merging process such as Ostwald ripening, and large nuclei grow further by absorbing smaller ones ($1+2\rightarrow\alpha$, $3+4\rightarrow\beta$, $5+6\rightarrow\gamma$, $7+8\rightarrow\delta$). Stage IV: if two similarly sized domains coexist, the merging process cannot continue because it is difficult for one domain to absorb the other, resulting in a complex boundary structure ($\alpha+\delta\rightarrow X$, $\beta+\gamma\rightarrow Y$).

a much higher concentration than that in the as-made solutions[20]; in other words, the initially grown metastable phases rapidly deplete the precursors in the surrounding area[21], a process that can delay further growth and transformation into the stable phase, eventually leaving the metastable phase intact. We heated a hcp PdH_x nanoparticle at 500 °C for 2 h in an in situ TEM heating system (Extended Data Fig. 8 and Methods) to induce phase transformation. Notably, the hcp nanoparticles maintained their structure even after annealing, indicating that hcp PdH_x is indeed a metastable phase and that the energy barrier between this phase and the stable fcc phase is quite high.

To gain deeper insights into the growth mechanism of hcp PdH_x, the detailed three-dimensional (3D) atomic arrangement of a PdH_x nanoparticle was investigated by performing atomic electron tomography (AET)[22,23]. A STEM tomography dataset was acquired at 33 different tilt angles ranging from −70° to 70°, and an atomic-resolution 3D tomogram was obtained using the GENFIRE algorithm (Methods)[24]. Individual atoms were clearly resolved in the reconstruction as local intensity maxima (Fig. 4a–c). The full 3D coordinates of individual atoms were traced by 3D Gaussian fitting at each local maximum, resulting in a 3D atomic model of the nanoparticle (Methods). To verify whether the nanoparticle indeed forms a hcp structure, local hexagonal stacking types were determined for each atom. As shown in Fig. 4d, each atom in a hcp crystal can have two different types of nearest-neighbour arrangements, namely, type A and type B. A perfect hcp crystal is expected to show alternating layers of type-A and type-B atoms. Interestingly, the measured nanoparticle was not a perfect single hcp crystal but exhibited a complex domain structure with different regions of ABAB and BABA stacking, as shown in Fig. 4a–c, e.

Nevertheless, the 3D connectivity of these different types of domains (the blue and red regions in Fig. 4e, exhibiting ABAB or BABA stacking, respectively) and their excellent agreement with the ideal hcp structure (Extended Data Fig. 9a) indicated that the nanoparticle indeed possessed hcp ordering.

Notably, the boundary between the two anti-phase hcp stacking domains (Fig. 4e) seems to be severely indented and irregularly shaped. This observation cannot be easily explained by coalescence events (aggregation or oriented attachment) because they usually result in sharp planar boundaries[8,10,25–27]. Instead, the presence of a complex boundary structure (Fig. 4f) indicates that the nanoparticle probably formed as a result of a multistep crystallization process that is more energetically favourable than direct crystallization[28–30], as described in Fig. 4g. Note that no diffraction peaks were observed at the early stage of growth (under approximately 1 s), indicating an amorphous phase, which further supports the multistep crystallization mechanism (Extended Data Fig. 10).

The stabilization of the subnanometre-sized particles of hcp PdH predicted by MC simulations corroborates the multistep crystallization process indicated by the AET experiment. Overall, the experimentally resolved atomic structure shows a domain size of approximately 1–2 nm (Extended Data Fig. 9a), which is similar to the nucleus diameter of 1.2 nm that favours the formation of hcp PdH (Fig. 2b, c). The transition from the amorphous phase to hcp crystal nuclei and subsequent growth of the crystalline parts by merging enables the formation of multidomain hcp PdH nanoparticles (Fig. 4g), which can grow larger than approximately a nanometre, the size limit for hcp PdH single crystals being more stable than that of fcc PdH.

In this study, we present a metastable hcp PdH_x. The unique environment in the liquid cell—namely, the limited quantity of Pd precursors and the continuous supply of H—resulted in the formation of the hcp phase. MC simulations reveal that an unexpected irregular distribution of interstitial H atoms, distinct from the predominant occupation at the octahedral interstitial sites, is the key to stabilizing nanoscale hcp PdH_x. Furthermore, insufficient Pd causes a multistep nucleation and growth pathway, deduced from in situ liquid cell TEM combined with AET, which maintains the intact metastable phase. The metastable hcp PdH_x exhibited a superior H capacity and stronger H binding than its fcc counterpart and its crystal structure was modulated (hcp or fcc) by adjusting the H and Pd concentrations inside the TEM liquid cell. This insight may provide a new route for designing and synthesizing novel energy storage materials. For example, by contrast with the conventional fabrication procedure based on a phase transformation driven by intercalation and dissolution, the synthesis of materials for H storage or Li-ion battery electrodes under a high concentration of H or Li could result in a new metastable phase. Such a synthesis of new metastable phases by the proposed approach will be pursued in future work.

Online content

Any methods, additional references, Nature Research reporting summaries, source data, extended data, supplementary information, acknowledgements, peer review information; details of author contributions and competing interests; and statements of data and code availability are available at https://doi.org/10.1038/s41586-021-04391-5.

1. Sun, W. et al. The thermodynamic scale of inorganic crystalline metastability. *Sci. Adv.* **2**, e1600225 (2016).
2. Martinolich, A. J. & Neilson, J. R. Toward reaction-by-design: achieving kinetic control of solid state chemistry with metathesis. *Chem. Mater.* **29**, 479–489 (2017).
3. Gopalakrishnan, J. Chimie douce approaches to the synthesis of metastable oxide materials. *Chem. Mater.* **7**, 1265–1275 (1995).
4. Chen, B.-R. et al. Understanding crystallization pathways leading to manganese oxide polymorph formation. *Nat. Commun.* **9**, 2553 (2018).
5. Aykol, M., Dwaraknath, S. S., Sun, W. & Persson, K. A. Thermodynamic limit for synthesis of metastable inorganic materials. *Sci. Adv.* **4**, eaaq0148 (2018).
6. Baldi, A., Narayan, T. C., Koh, A. L. & Dionne, J. A. In situ detection of hydrogen-induced phase transitions in individual palladium nanocrystals. *Nat. Mater.* **13**, 1143–1148 (2014).
7. Griessen, R., Strohfeldt, N. & Giessen, H. Thermodynamics of the hybrid interaction of hydrogen with palladium nanoparticles. *Nat. Mater.* **15**, 311–317 (2016).
8. Yuk, J. M. et al. High-resolution EM of colloidal nanocrystal growth using graphene liquid cells. *Science* **336**, 61–64 (2012).
9. Schneider, N. M. et al. Electron–water interactions and implications for liquid cell electron microscopy. *J. Phys. Chem. C* **118**, 22373–22382 (2014).
10. Park, J. et al. 3D structure of individual nanocrystals in solution by electron microscopy. *Science* **349**, 290–295 (2015).
11. Sachs, C. et al. Solubility of hydrogen in single-sized palladium clusters. *Phys. Rev. B* **64**, 075408 (2001).
12. Moore, W. J. Jr & Pauling, L. The crystal structures of the tetragonal monoxides of lead, tin, palladium, and platinum. *J. Am. Chem. Soc.* **63**, 1392–1394 (1941).
13. Zhou, X., Zimmerman, J. A., Wong, B. M. & Hoyt, J. J. An embedded-atom method interatomic potential for Pd–H alloys. *J. Mater. Res.* **23**, 704–718 (2008).
14. Algara-Siller, G. et al. Square ice in graphene nanocapillaries. *Nature* **519**, 443–445 (2015).
15. Yang, X., Li, H., Ahuja, R., Kang, T. & Luo, W. Formation and electronic properties of palladium hydrides and palladium-rhodium dihydride alloys under pressure. *Sci. Rep.* **7**, 3520 (2017).
16. Walter, J., Heiermann, J., Dyker, G., Hara, S. & Shioyama, H. Hexagonal or quasi two-dimensional palladium nanoparticles—tested at the Heck reaction. *J. Catal.* **189**, 449–455 (2000).
17. Park, J. H. et al. Control of electron beam-induced Au nanocrystal growth kinetics through solution chemistry. *Nano Lett.* **15**, 5314–5320 (2015).
18. Ross, F. M. *Liquid Cell Electron Microscopy* (Cambridge Univ. Press, 2017).
19. Bakalis, E. et al. Complex nanoparticle diffusional motion in liquid-cell transmission electron microscopy. *J. Phys. Chem. C* **124**, 14881–14890 (2020).
20. Loh, N. D. et al. Multistep nucleation of nanocrystals in aqueous solution. *Nat. Chem.* **9**, 77–82 (2017).
21. Nielsen, M. H., Aloni, S. & De Yoreo, J. J. In situ TEM imaging of $CaCO_3$ nucleation reveals coexistence of direct and indirect pathways. *Science* **345**, 1158–1162 (2014).
22. Yang, Y. S. et al. Deciphering chemical order/disorder and material properties at the single-atom level. *Nature* **542**, 75–79 (2017).
23. Zhou, J., Yang, Y., Ercius, P. & Miao, J. Atomic electron tomography in three and four dimensions. *MRS Bull.* **45**, 290–297 (2020).
24. Pryor, A. Jr et al. GENFIRE: a generalized Fourier iterative reconstruction algorithm for high-resolution 3D imaging. *Sci. Rep.* **7**, 10409 (2017).
25. Li, D. et al. Direction-specific interactions control crystal growth by oriented attachment. *Science* **336**, 1014–1018 (2012).
26. Lange, A. P. et al. Dislocation mediated alignment during metal nanoparticle coalescence. *Acta Mater.* **120**, 364–378 (2016).
27. Kim, B. H. et al. Critical differences in 3D atomic structure of individual ligand-protected nanocrystals in solution. *Science* **368**, 60–67 (2020).
28. Zhang, T. H. & Liu, X. Y. How does a transient amorphous precursor template crystallization. *J. Am. Chem. Soc.* **129**, 13520–13526 (2007).
29. Lee, J., Yang, J., Kwon, S. G. & Hyeon, T. Nonclassical nucleation and growth of inorganic nanoparticles. *Nat. Rev. Mater.* **1**, 16034 (2016).
30. Guo, C., Wang, J., Li, J., Wang, Z. & Tang, S. Kinetic pathways and mechanisms of two-step nucleation in crystallization. *J. Phys. Chem. Lett.* **7**, 5008–5014 (2016).

Methods

Precursor solution

The palladium precursor solution was prepared by dissolving sodium tetrachloropalladate(II) (Na_2PdCl_4, Aldrich) and isopropyl alcohol (Junsei) in distilled water[31]. Five different Pd precursor solutions with concentrations of 3.67, 10, 18, 36.7 and 73 mM were used. AET was performed with a particle generated in the 3.67 mM precursor solution. Isopropanol was used as a hydroxyl radical scavenger to minimize the probability of dissolution of palladium nanoparticles. The molar concentration of isopropanol in the aqueous solution was 0.1 M (refs. [9,32]).

Liquid TEM cell

The GLC was fabricated following previous reports[8]. Multilayer graphene, which was purchased from Graphene Square Incorporation, was adopted to increase the durability of the GLC under bombardment with electrons accelerated at a few hundred kilovolts. Heating experiments for the GLC were conducted with a commercial heating holder, Gatan Heating In-Situ Holder 652. SLC experiments were conducted with a commercial in situ liquid holder, Protochips Poseidon 210, in which both the window and spacer were 50 nm thick. In liquid flow at the SLC, liquid was flowed at a rate of 30 μl h^{-1} by using a syringe pump.

TEM

Electron-beam-induced PdH_x nanoparticle growth in a liquid was traced in real time with a Titan TEM (FEI Titan 80-300) operated at 300 kV, which was equipped with a OneView charge-coupled device (CCD) camera (Gatan). This TEM was also used to irradiate electrons in a liquid cell to generate particles for ex situ analysis. High-resolution TEM (HR-TEM) and HR-STEM images of the particles generated in the GLC with 3.67 mM Pd solution under a medium EDR were acquired with a double Cs-corrected Titan Themis TEM (FEI) operated at 300 kV, which was equipped with a monochromator and Gatan Quantum 966 electron energy loss (EEL) spectrometer. HR-TEM images of the particles formed under other conditions were obtained using the aforementioned Titan TEM.

Monochromated EEL spectra of the hcp particles formed inside the SLC were acquired using a Titan Themis TEM operated at 80 kV (refs. [6,33]). EDS analysis was conducted with a Talos TEM (FEI Talos F200X) operated at 200 kV equipped with a Super-X EDS system using four silicon drift detectors.

Background subtraction and smoothing of EELS data

A background function based on the well-known power model[34] was fitted to the region outside the energy range of the PdH_x nanoparticle plasmon peak. The fitted background was subtracted from the raw EELS data. Smoothing with a Gaussian kernel of $\sigma = 0.60$ eV was subsequently applied to minimize the noise effect and clarify the plasmon peak.

EDR

The EDR was set as the electron flux, the number of electrons irradiated per unit area per unit time (e^- Å^{-2} s^{-1}). EDR is given as

$$\mathrm{EDR} = \frac{I}{q_e \pi R^2} \quad (1)$$

where I is the screen current (1 A = 1 C s^{-1}), R is the electron beam radius (Å) and q_e is the elementary charge ($1.602176634 \times 10^{-19}$ C $(e^-)^{-1}$). The screen current I and the beam radius R were measured and displayed in TEM user interface software. The number of electrons irradiated on the sample per unit time (s) was obtained by dividing the screen current I by the elementary charge q_e. The electron beam illumination area was calculated as πR^2 because the electron beam has a circular shape. The EDR was then expressed as the number of electrons irradiated on the sample per unit time divided by the beam illumination area, as described in equation (1) (ref. [35]).

We adopted three different EDRs, high, medium and low, to investigate the effect of EDR on the formation of hcp PdH_x nanoparticles. High EDR corresponds to 9,934 e^- Å^{-2} s^{-1} (screen current 5 nA with beam radius 100 nm), whereas medium EDR is 675 e^- Å^{-2} s^{-1} (screen current 14.8 nA with beam radius 660 nm) and low EDR is 39 e^- Å^{-2} s^{-1} (screen current 15.6 nA with beam radius 2.81 μm) (Extended Data Fig. 3c). Along with the three EDRs, we adopted different irradiation times for different EDRs. The irradiation time was only a few minutes for the high EDR, and we were able to acquire high-resolution in situ images. For the medium and low EDRs, we irradiated the samples with electron beams for 20 and 30 min, respectively, to ensure the formation of nanoparticles, as we were not able to obtain high-resolution images during irradiation owing to the low electron intensity in each pixel of the CCD camera at high magnification. However, we performed only ex situ analysis for the SLC experiments because the dynamic motion of nanoparticles, which was possibly caused by window charging, hindered us from acquiring high-resolution in situ images even at the high EDR.

Molar volume calculation

The molar volume of the nanoparticles was obtained from the lattice constants, which were calculated from the DPs of the HR-TEM and HR-STEM images of nanoparticles along the $[1\bar{2}1\bar{3}]$, $[\bar{2}110]$ and $[01\bar{1}1]$ zone axes. We used the crystallographic relationship formula of the hcp structure below, which describes the interplanar distance between adjacent (hkl) Miller planes, d_{hkl}, to derive the lattice constants[36]:

$$\frac{1}{d_{hkl}^2} = \frac{4}{3}\left(\frac{h^2 + hk + k^2}{a^2}\right) + \frac{l^2}{c^2}$$

The lattice constant a was directly calculated from the $(1\bar{1}00)$ planes, and the lattice constant c was calculated from the $(1\bar{1}01)$ planes and the aforementioned $(1\bar{1}00)$ planes for the particle along the $[1\bar{2}1\bar{3}]$ zone axis. For the particle along the $[\bar{2}110]$ zone axis, the lattice constants a and c were directly calculated from the $(0\bar{1}10)$ and (0002) planes, respectively. For the particle along the $[01\bar{1}1]$ zone axis, the lattice constants a and c were calculated by considering the $(1\bar{1}01)$, $(0\bar{1}12)$ and $(\bar{2}110)$ planes altogether. Notably, some particles had lattice constants quite different from those of most particles. Specifically, some particles had far higher c and/or a values, whereas others had far lower values. These differences were attributed to the deviation in the number of H atoms in the particles. As the hcp palladium hydride nanoparticles formed explosively, some particles might have been formed in non-average surroundings, that is, some might have been exposed to an excess of H radicals, whereas others might not. In addition, the particle diameter was set as the geometric mean of the lengths of the major axis and minor axis of a particle, assuming the particle to be an ellipsoid.

In situ d-spacing tracking

The plane index of the diffraction spot and the corresponding d-spacing, acquired when the particle was aligned along the zone axis, were obvious, as plane information was manifested in the zone axis pattern. When the particle was not along the zone axis, the diffraction spot of the particle was assigned to a plane index considering the continuity of fringes and the degree of proximity between the aforementioned d-spacing value in the video and the average interplanar distance measured ex situ.

Bulk scale PdH_x/C preparation through e-beam irradiation

To synthesize PdH_x nanoparticles through irradiation with an electron beam in a batch reactor outside the TEM, 1 l of 3.67 mM Na_2PdCl_4 was prepared in a 0.1 M isopropyl alcohol aqueous solution. Then, carbon black was added to the reaction solution, which was homogeneously mixed under ultrasonication for 10 min at room temperature. Thereafter, the reaction vessel was placed under electron beam irradiation at an EDR of 1.9×10^{-3} e^- Å^{-2} s^{-1} for several minutes. The resulting solution

was filtered with distilled water several times and black precipitates were obtained.

X-ray diffraction

X-ray diffraction analysis was performed at room temperature in the 2θ range of 10–90° on a D8 Advance (Bruker AXS, Germany) diffractometer equipped with a LynxEye line detector using Cu Kα radiation (wavelength λ = 1.5418 Å) at 40 kV and 40 mA and a scanning rate of 0.5° min^{-1} with a step size of 0.02°.

To prove that the lattice of Pd/C was expanded relative to that of pristine Pd, an internal standard of Si powder (NIST SRM 640e) was used. The lattice parameters of Pd/C were refined with the Le Bail method[37] using TOPAS software (Bruker AXS, Germany)[38]; the lattice parameter of Si was fixed to a = 5.431179 Å.

AET

For data acquisition, a tomographic tilt series of a PdH_x nanoparticle was obtained using a Titan Themis TEM. In high-angle annular dark-field scanning transmission electron microscopy (HAADF-STEM) mode, 33 tilt series images of 1,024 × 1,024 pixels were obtained between −70.0° and +70.0° with a 35.50 pm pixel size. Ten images were consecutively acquired for each tilt angle with a 3 µs dwell time. A linear drift constant was estimated from consecutive images and corrected for each angle. Then, a scan distortion correction was applied to correct the image distortions owing to slight misalignment between the x and y directions of the scan coil based on a reference image of the Si [110] zone axis taken under the same measurement conditions.

For image denoising, HAADF-STEM images suffer from Poisson–Gaussian noise. The Poisson and Gaussian noise parameters were estimated from the image statistics of ten consecutively acquired images, and sparsity-based transform domain denoising (BM3D) was applied, as described in refs. [22–24,39,40].

For GENFIRE reconstruction, after denoising, the projections were aligned based on the common-line and centre-of-mass methods for alignment along the tilt axis direction and perpendicular to the tilt axis direction, respectively[22,24,40–42]. Tomographic reconstruction was performed using GENFIRE for the aligned tilt-series images[22,24,40–42] with an oversampling ratio of 4 and an interpolation radius of 0.1 pixels. To improve the quality of the reconstruction, an angular refinement process was applied to minimize the discrepancy between the forward-projected projections of the reconstruction volume and the experimental projections[24]. The final reconstruction obtained after the refinement process showed a clear atomic-resolution internal structure.

The 3D atomic coordinates of all atoms in the nanoparticle were determined by fitting a 3D Gaussian function on a 5 × 5 × 5 voxel volume near each local maximum. The fittings were performed in descending order from the highest intensity local maximum, and a minimum distance constraint of 2.4 Å was enforced during the process. However, owing to the atom elongation effect resulting from the missing wedge and a slight imperfection of the reconstruction, several connected intensity blobs were not properly traced owing to a failure to properly identify the local maxima. To locate the untraced atoms, the reconstruction volume was sliced along the hexagonal c axis at each atomic layer, and the local maxima in each slice were identified. Then, the same Gaussian fitting procedure was repeated using the new local maxima in descending order, still enforcing the same minimum distance constraint. After this process, a final 3D atomic model of 9,868 atoms was obtained.

To analyse the 3D atomic structure, proper hcp lattice sites must be assigned for each atom. To begin the assignment procedure, the hcp lattice vectors for the nanoparticle were roughly estimated from the peak positions in the 3D Fourier-transformed reconstruction volume. Then, an atom closest to the mean position of the given 3D atomic coordinates was selected and assigned to the origin of the hcp lattice. From the starting atom, the positions of the 12 nearest-neighbor (NN) atoms and corresponding NN hcp lattice sites were calculated. At each NN position, a sphere was drawn with a radius of one quarter of the NN distance. If an atom was encompassed by the sphere, the atom was assigned to the lattice site corresponding to the NN position. This process was continued for all newly assigned hcp lattice sites and repeated until there were no newly assigned sites. Note that an atom in a hcp structure can have two different types of NN structure, as described in Fig. 4d. To determine the NN structure to which the starting atom belonged, the process above was repeated twice for two different NN structures, and the one that resulted in a larger number of assigned hcp sites was chosen. After assigning hcp lattice sites for all available atoms, the hcp lattice vectors were fitted to minimize the error between the measured atomic positions and the corresponding lattice positions of the fitted hcp lattice. The entire process described above was continuously repeated with the newly obtained hcp lattice vectors until the lattice vectors stopped changing.

For domain identification, in the initial trial, hcp lattice assignment and lattice parameter fitting were performed assuming the entire nanoparticle to be a hcp single crystal, resulting in the initial hcp lattice vectors. However, the nanoparticle is not guaranteed to consist of a single crystal. Therefore, the local lattice assignments and fittings described above were individually performed for all the atoms within the nanoparticle to check their NN ordering. For the local fitting, only the atoms within the distance of the mean of the NN and next-nearest-neighbour (NNN) distance, which was determined from the hcp fitting of the entire nanoparticle, were used. From the local fittings, the local lattice constant and NN structure type (Fig. 4d, named type A or type B here) were obtained for each atom. After local fitting, all the atoms were assigned to the closest atomic layer perpendicular to the hexagonal c axis (Fig. 4e). Then, type-A atoms in odd-numbered layers and type-B atoms in even-numbered layers were classified as ABAB stacking, and the opposite cases were classified as BABA stacking. As shown in Fig. 4e, atoms with the same stacking type formed clusters.

To identify the connected clusters, we performed a local connectivity analysis. First, we selected a starting atom, around which we drew a sphere whose radius was the mean of the NN and NNN distances. Then, we counted how many of the atoms within the sphere shared the same stacking type as the selected atom. If the number was larger than a certain threshold, the selected atom was considered to be within a connected domain, and a specific domain identifier was assigned to it. In this case, we added atoms with the same stacking type as the selected atom to the potential domain atom list, and we repeated the process for all the newly added atoms in the list. For all the atoms that fulfilled the numerical threshold, the same domain identifier was assigned. For atoms that did not meet the numerical threshold, we checked whether all of the atoms in their local sphere had the same atom type. If that was the case, we assigned the same domain identifier to the atom. Otherwise, the atom was marked as a non-domain atom (not belonging to any domain). We repeated the procedure above until there were no newly added atoms in the potential domain atom list. Finally, the collection of atoms with the same domain identifier formed a domain. We repeated this entire process starting with each other atom with a different domain identifier. After performing the process for all available atoms, all connected domains in the nanoparticle could be identified. Individual hcp lattices could be separately assigned and fitted to each identified domain to correctly determine their lattice constants.

We tested several different numerical thresholds for this analysis, and a numerical threshold of 7 yielded the largest number of atoms successfully assigned to hcp lattice sites after separate domain fittings. Using this threshold, we found 5 connected domains in the nanoparticle, containing 3,392, 3,552, 9, 7 and 2 atoms. The remaining 2,906 atoms were not assigned to any domain. Finally, hcp lattice constants of a = 2.9539 Å and c = 4.6692 Å were obtained by averaging each domain's lattice constants, weighted by the number of atoms.

DFT calculations

The stabilities of fcc PdH_x and hcp PdH_x were compared using DFT calculations, which were carried out using the Quantum-ESPRESSO package[43,44] with PBEsol[45] as an exchange-correlation functional and the projector augmented wave[46] pseudopotentials generated by the atomic code[47]. The PBEsol functional was used because it accurately reproduces the experimental lattice parameters of PdH[48], which is important in this study. The planewave cutoff energy was set to 60 Ry. Then 16 × 16 × 16 and 23 × 23 × 14 regular *k*-point meshes were used to sample the Brillouin zone of the unit cell of fcc Pd(H) and hcp Pd(H), respectively, with a Marzari–Vanderbilt cold smearing[49] of 0.02 Ry. The lattice constants of the fcc and hcp Pd and PdH crystals were varied until the optimized lattice parameters were obtained (Extended Data Fig. 1a). We performed phonon calculations within the density functional perturbation theory[50] implemented in the Quantum-ESPRESSO package. For the phonon calculations, 4 × 4 × 4 and 6 × 6 × 4 *q*-point meshes were used for fcc Pd(H) and hcp Pd(H), respectively. The inclusion of the zero-point energy through phonon calculations (Extended Data Fig. 11) is critical for a proper comparison of the relative stabilities of octahedral versus tetrahedral occupation of the Pd interstitial sites by H atoms[48,51]. The hcp-tetrahedral PdH was simulated in the wurtzite structure.

To understand the surface effect in a PdH_x nanoparticle, a two-dimensional slab model, infinite in the *a*–*b* plane and finite along the *c* axis, was used because the full description of a 3D nanoparticle is computationally demanding. To suppress the interaction between periodic images along the *c* axis, a vacuum region of at least 8 Å was inserted. Owing to the symmetric arrangement of the atoms, no net dipole moment developed, and the error caused by the periodic images was minimal. The energy changes during layer-by-layer growth of the fcc and hcp PdH slabs were compared (Extended Data Fig. 7). Alternating Pd and H layers were added, and the formation energy was calculated with respect to fcc Pd and H_2.

MC simulation using the EAM potential model

The stability of bulk PdH_x crystals with different crystal packing was analysed using the classical interatomic potential for Pd–H based on the EAM, which predicts the lattice constants and elastic properties of PdH_x (ref. [13]). The total energy of the bulk PdH_x crystals was calculated using the EAM potential at the DFT-optimized geometry for hcp/fcc PdH_x. The DFT-optimized lattice constants were scaled to match the experiments. The H atoms were placed exactly at the octahedral or tetrahedral interstitial sites of the Pd atom unit cells. For tetrahedral occupation, H atoms in the equivalenced PdH crystal would fill half of all of the tetrahedral sites, which were modelled as zinc-blende and wurtzite structures for fcc PdH and hcp PdH, respectively.

An MC simulation of finite-sized PdH nanoparticles was performed to understand the effects of particle size and crystal packing on the relative thermodynamic stability and the internal structure of the nanoparticles. The radii of the nanoparticles were varied from 6 to 30 Å, and the Pd atoms were prepared with two different crystal packings (fcc/hcp). The Pd atoms in the fcc/hcp nanoparticles were positioned with ideal fcc and hcp structures using the lattice constants of fcc/hcp PdH obtained from DFT calculations (scaled to match the experimental lattice constant). The lattice constant of partially hydrogenated PdH_x was obtained by linearly scaling the lattice constants of PdH and pure Pd crystals with fcc/hcp structures. In addition, MC simulations were performed to construct a local H concentration map in the experimentally obtained hcp PdH nanoparticle, which used the 3D atomic coordinates of Pd atoms obtained from the AET experiment.

Each MC move involved the random displacement of H atoms in the fixed Pd nanocrystals. Initially, all H atoms were randomly placed inside the nanoparticles. Each new H atom position was accepted or rejected by Metropolis criteria in the constant volume and temperature (NVT) ensemble, with the system temperature set at 300 K. To ensure that H atoms remained in the nanoparticle, new H positions that were not within a cut-off distance of 2.5 Å from any Pd atoms were rejected. The total energy of the system was equilibrated after a half million accepted MC moves for the smallest nanoparticles. Each nanoparticle was simulated until 5 million MC moves were accepted. The trajectory of the H atom positions was saved for every 100 successful MC moves. The total energy of the nanoparticles and the H occupancy at different interstitial sites (Fig. 2 and Extended Data Figs. 2, 9b) were statistically analysed by averaging the last 1,000 snapshots from each simulation trajectory.

Data availability

The data that support the findings of this study are available from the corresponding author upon request.

Code availability

MC simulation code and data for the nanoparticle stability analysis are available at GitHub repository https://github.com/scychon/HCP-PdH. Atomic electron tomography code and data are available at http://mdail.kaist.ac.kr/HCP-PdH.

31. Lim, B., Xiong, Y. & Xia, Y. A water-based synthesis of octahedral, decahedral, and icosahedral Pd nanocrystals. *Angew. Chem. Int. Edn* **46**, 9279–9282 (2007).
32. Buxton, G. V., Greenstock, C. L., Helman, W. P. & Ross, A. B. Critical review of rate constants for reactions of hydrated electrons, hydrogen atoms and hydroxyl radicals ($\cdot OH/\cdot O^-$) in aqueous solution. *J. Phys. Chem. Ref. Data* **17**, 513–886 (1988).
33. Jung, H. J. et al. Spatial variation of available electronic excitations within individual quantum dots. *Nano Lett.* **13**, 716–721 (2013).
34. Egerton, R. F. *Electron Energy-Loss Spectroscopy in the Electron Microscope* (Springer Science & Business Media, 2011).
35. Woehl, T. J., Evans, J. E., Arslan, I., Ristenpart, W. D. & Browning, N. D. Direct in situ determination of the mechanisms controlling nanoparticle nucleation and growth. *ACS Nano* **6**, 8599–8610 (2012).
36. Hammond, C. *The Basics of Crystallography and Diffraction* Vol. 214 (Oxford, 2001).
37. Duroy, H. & Fourquet, J. Ab-initio structure determination of $LiSbWO_6$ by x-ray powder diffraction. *Mat. Res. Bull.* **23**, 447–452 (1988).
38. Bruker AXS, TOPAS v5. General profile and structure analysis software for powder diffraction data—user's manual (Bruker AXS,Karlsruhe, Germany, 2014).
39. Dabov, K., Foi, A., Katkovnik, V. & Egiazarian, K. Image denoising by sparse 3-D transform-domain collaborative filtering. *IEEE Trans. Image Process.* **16**, 2080–2095 (2007).
40. Tian, X. et al. Correlating the three-dimensional atomic defects and electronic properties of two-dimensional transition metal dichalcogenides. *Nat. Mater.* **19**, 867–873 (2020).
41. Scott, M. C. et al. Electron tomography at 2.4-ångström resolution. *Nature* **483**, 444–447 (2012).
42. Chen, C. C. et al. Three-dimensional imaging of dislocations in a nanoparticle at atomic resolution. *Nature* **496**, 74–77 (2013).
43. Giannozzi, P. et al. QUANTUM ESPRESSO: a modular and open-source software project for quantum simulations of materials. *J. Phys. Condens. Matter* **21**, 395502 (2009).
44. Giannozzi, P. et al. Advanced capabilities for materials modelling with QUANTUM ESPRESSO. *J. Phys. Condens. Matter* **29**, 465901 (2017).
45. Perdew, J. P. et al. Restoring the density-gradient expansion for exchange in solids and surfaces. *Phys. Rev. Lett.* **100**, 136406 (2008).
46. Blöchl, P. E. Projector augmented-wave method. *Phys. Rev. B* **50**, 17953–17979 (1994).
47. Dal Corso, A. Pseudopotentials periodic table: from H to Pu. *Comput. Mater. Sci.* **95**, 337–350 (2014).
48. Houari, A., Matar, S. F. & Eyert, V. Electronic structure and crystal phase stability of palladium hydrides. *J. Appl. Phys.* **116**, 173706 (2014).
49. Marzari, N., Vanderbilt, D., De Vita, A. & Payne, M. C. Thermal contraction and disordering of the Al(110) surface. *Phys. Rev. Lett.* **82**, 3296–3299 (1999).
50. Baroni, S., de Gironcoli, S., Dal Corso, A. & Giannozzi, P. Phonons and related crystal properties from density-functional perturbation theory. *Rev. Mod. Phys.* **73**, 515–562 (2001).
51. Long, D. et al. Accounting for the thermo-stability of PdH_x (x = 1–3) by density functional theory. *Int. J. Hydrog. Energy* **43**, 18372–18381 (2018).
52. Arblaster, J. W. Crystallographic properties of palladium. *Platin. Met. Rev.* **56**, 181–189 (2012).
53. Schirber, J. E. & Morosin, B. Lattice constants of β–PdH_x and β–PdD_x with x near 1.0. *Phys. Rev. B* **12**, 117–118 (1975).
54. Errea, I., Calandra, M. & Mauri, F. First-principles theory of anharmonicity and the inverse isotope effect in superconducting palladium-hydride compounds. *Phys. Rev. Lett.* **111**, 177002 (2013).
55. Kobayashi, K. et al. Discovery of hexagonal structured Pd-B nanocrystals. *Angew. Chem. Int. Edn* **56**, 6578–6582 (2017).

56. Chen, L. et al. Metal boride better than Pt: HCP Pd_2B as a superactive hydrogen evolution reaction catalyst. *Energy Environ. Sci.* **12**, 3099–3105 (2019).
57. Politano, A., Chiarello, G. & Spinella, C. Plasmon spectroscopy of graphene and other two-dimensional materials with transmission electron microscopy. *Mater. Sci. Semicond. Process.* **65**, 88–99 (2017).
58. Schneider, N. M. *Radiolysis.* GitHub https://github.com/NMSchneider/Radiolysis (2015).
59. Kwon, S. G. & Hyeon, T. Formation mechanisms of uniform nanocrystals via hot-injection and heat-up methods. *Small* **7**, 2685–2702 (2011).

Acknowledgements This research was supported by the National Research Foundation (grant nos. 2018M3D1A1058793, 2015M1A2A2074688, 2018M1A2A2061975, 2021M3H4A1A02042948, 2019R1F1A1058236, 2020R1C1C1006239, 2020R1F1A1060331 and 2019M3E6A1064877), the Korea Institute of Science and Technology (grant no. 2E30201), the KAIST-funded Global Singularity Research Program (M3I3) and the Institute for Basic Science (grant no. IBS-R006-D1).

Author contributions J.H., J.-H.B., S.J.Y. and D.W.C. conceived the research. J.H. and J.-H.B. designed and performed the experiments and analysed the results. H.J. and Y.Y. conducted AET. H.-Y.P. and S.L. contributed to the synthesis and analysis of nanoparticles. S.J.H., H.C., B.H. and Y.-S.L. carried out the DFT calculations and analysis. C.Y.S. performed the MC calculations and analysis. M.K.C., Juyoung K. and H.B. performed the TEM and EELS acquisition and analysis, whereas S.-C.K. performed the Rietveld refinement analysis. Joodeok K., Y.S., T.H. and J.P. interpreted the dynamics of the nanoparticles in liquids. K.L. and S.H.K. analysed the in situ TEM images. H.J., J.-Y.S., H.-K.R., K.H.L., H.-S.K., K.Y.C., C.W.Y., J.-P.A., G.H.K. and S.J. discussed and commented on the results. J.H., J.-H.B., H.J., C.Y.S., Y.Y., Y.-S.L., S.J.Y. and D.W.C. wrote the manuscript. C.Y.S., Y.Y., Y.-S.L., S.J.Y. and D.W.C. supervised the project. All authors approved the final version of the manuscript for submission.

Competing interests The authors declare no competing interests.

Additional information
Supplementary information The online version contains supplementary material available at https://doi.org/10.1038/s41586-021-04391-5.
Correspondence and requests for materials should be addressed to Chang Yun Son, Yongsoo Yang, Young-Su Lee, Sung Jong Yoo or Dong Won Chun.
Peer review information *Nature* thanks Damien Alloyeau and the other, anonymous, reviewer(s) for their contribution to the peer review of this work.

a

	Experimental lattice parameters at 300 K	DFT-optimized lattice parameters		Estimated lattice parameters at 300 K	
	a (Å)	a (Å)	c (Å)	a (Å)	c (Å)
fcc Pd	3.8905[52]	3.883			
fcc PdH	4.104[53,54]	4.078			
hcp Pd		2.728	4.563	2.733	4.571
hcp PdH		2.871	4.785	2.889	4.815

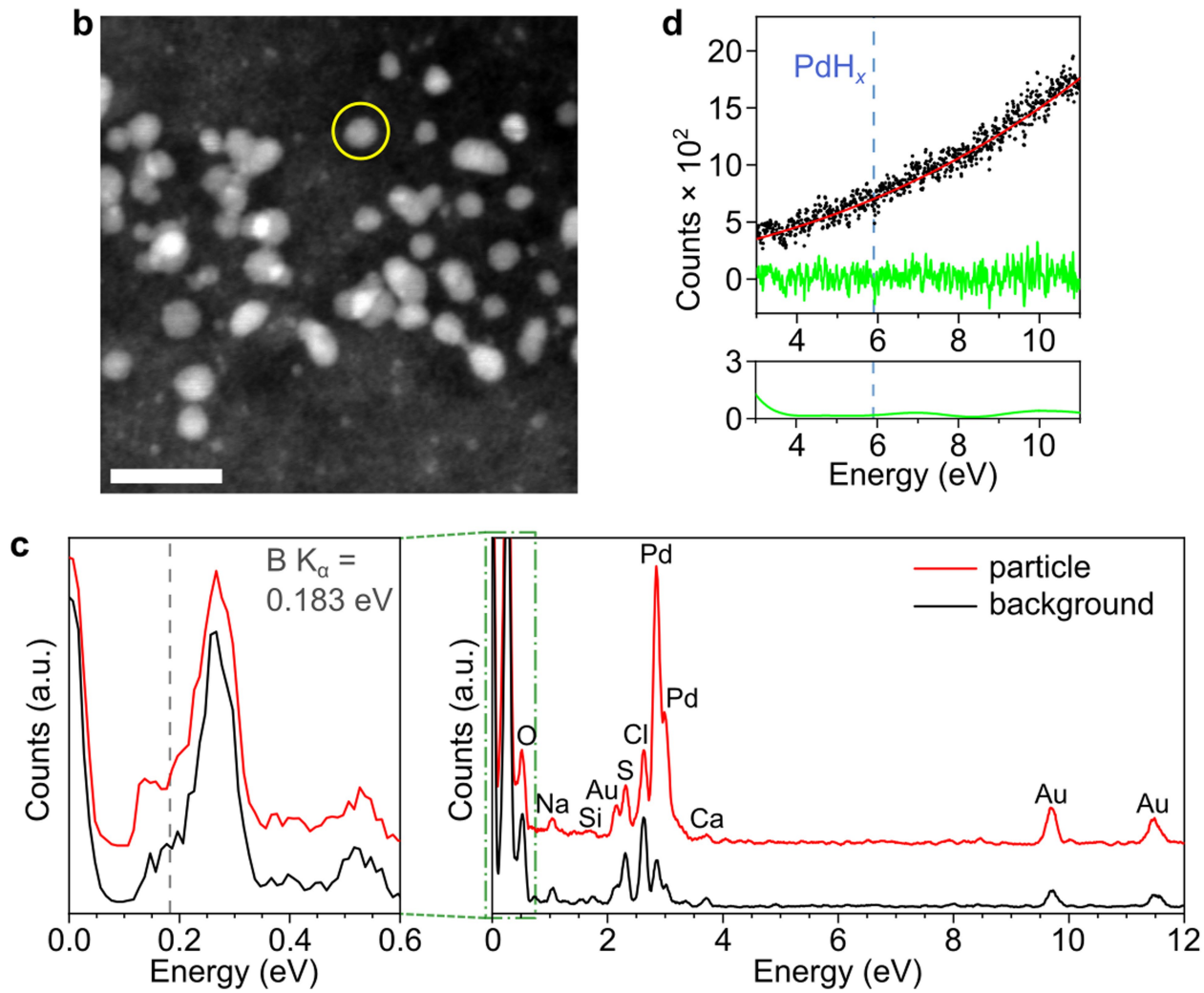

Extended Data Fig. 1 | See next page for caption.

Extended Data Fig. 1 | Estimation of the lattice parameters of hcp PdH_x and chemical analysis of hcp particles. a, The DFT-optimized and experimental lattice parameters of fcc PdH_x are used to improve the prediction of the lattice parameters of hitherto unknown hcp PdH_x. The lattice parameter of fcc Pd at 300 K is well-known[52], but the lattice parameter of stoichiometric fcc PdH at 300 K is not known. Hence, the lattice parameter of PdH at 77 K reported by Schirber et al.[53] was used, and then, the thermal expansion discussed by Errea et al.[54] was applied. As summarized in the table, the experimental lattice parameters at 300 K were found to be slightly larger than the DFT-optimized values. The estimated lattice parameters of the hcp structures were obtained by multiplying the DFT values by the ratio a (300 K, exp)/a (DFT) for the respective compositions in the fcc structure. **b**, Ex situ HAADF-STEM image of hcp nanoparticles, marked with a yellow circle where the EDS spectrum of a hcp particle in **c** was acquired (same area where the EDS maps in Fig. 1h were obtained). Scale bar, 20 nm. **c**, EDS spectra of one of the nanoparticles (red) and a background area (black). While some residues of the precursor solution and contamination are present in the sample, the difference between the spectra of the particle and background shows that the particle consists solely of Pd. The magnified spectra (left) within the range of the full spectrum (right) denoted by the green dash-dotted box indicate the absence of boron, hence excluding the possibility that Pd–B formed in the GLC[55,56]. **d**, EEL spectra acquired from a background Si_3N_4 window. While the black dots and red line show the raw data and fitted background, respectively, the green lines represent the background-removed EEL spectrum (top box) and its denoised version (bottom box). The SLC was used instead of the GLC to prevent overlap between the plasmon peaks of Pd and graphene[57]. The absence of a peak at approximately 5.9 eV indicates that the peak that appeared in the hcp particle originated from the particle itself.

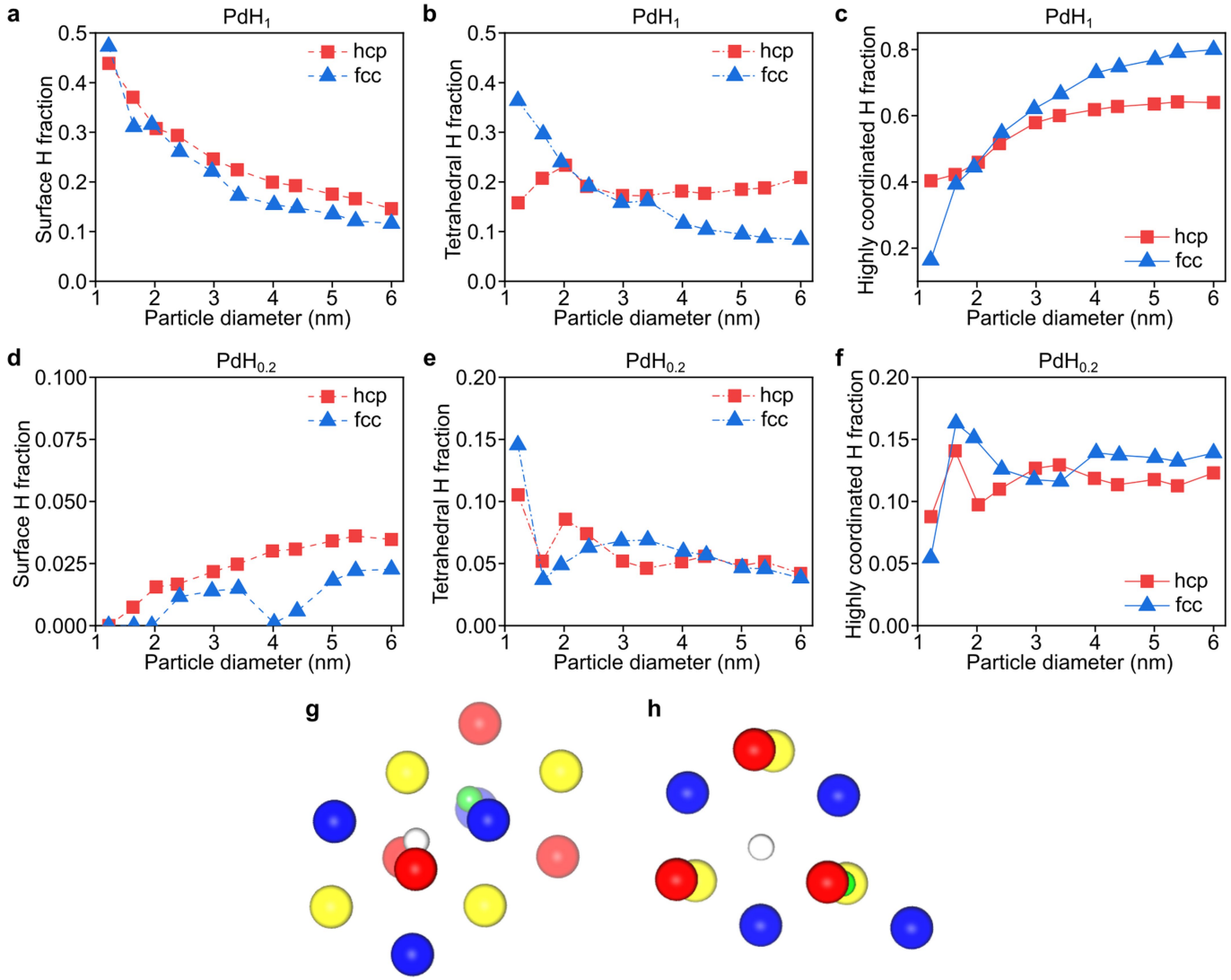

Extended Data Fig. 2 | H occupancy in finite-sized PdH_x nanoparticles with different crystal packing. a–**f**, Partitioning of H atoms in PdH nanoparticles with different particle sizes and crystal packing with these H atoms occupying various Pd interstitial sites in nanoparticles with high H content ($x = 1$) (**a**–**c**) and low H content ($x = 0.2$) (**d**–**f**), respectively. The H sites are categorized by the number of coordinating Pd atoms, where surface (**a**, **d**), tetrahedral (**b**, **e**), or highly occupied (trigonal bipyramidal/octahedral) (**c**, **f**) represent 0–3, 4, or 5–6 Pd atoms within the coordinating distance from the H atom, respectively. **g**, **h**, Representative coordination structure of PdH showing H atoms in the octahedral (white) and tetrahedral (green) interstitial sites formed by fcc (**g**) and hcp (**h**) crystal packing. Pd atoms are shown as large spheres, and the colors represent different Pd layers. The 1-4-layer overlap (ABCA') in the fcc Pd structure provides extra stabilization for octahedral H atoms, while the 1-3-layer overlap (ABA') in the hcp Pd structure provides extra stabilization to tetrahedral (T) and trigonal bipyramidal (TB) H atoms, resulting in distinct H atom occupancy, especially in small nanoparticles. At a diameter of 1.2 nm, almost half of the H atoms reside on the surface, regardless of the crystal packing.

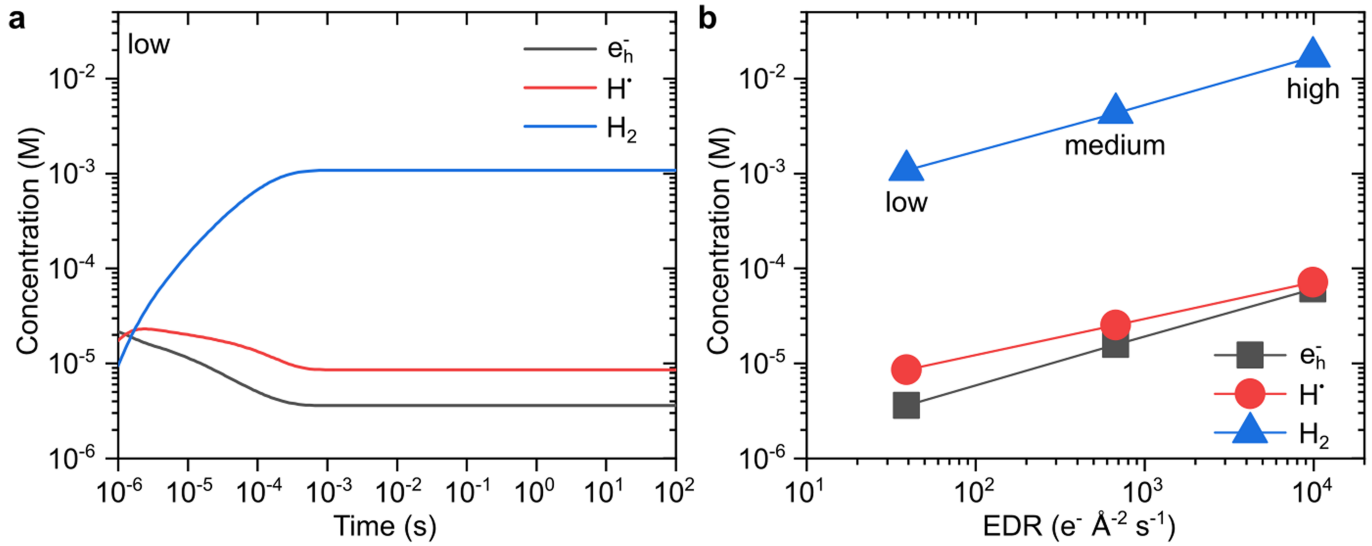

c

Condition	Screen current (I)	Beam radius (R)	Magnification	EDR
High	5 nA (± 0.6%)	100 nm	630,000 ×	9,934 e^- Å^{-2} s^{-1}
Medium	14.8 nA (± 0.7%)	660 nm	105,000 ×	675 e^- Å^{-2} s^{-1}
Low	15.6 nA (± 0.6%)	2.81 μm	25,500 ×	39 e^- Å^{-2} s^{-1}

Extended Data Fig. 3 | Concentration of radiolysis products as a function of time and EDR. a, Evolution over time of the concentrations of e_h^-, H•, and H_2 under low EDR. **b**, Steady-state concentrations of e_h^-, H•, and H_2 under low, medium, and high EDRs. The concentrations were calculated assuming uniform irradiation of the neat water using a publicly available code[9,58]. In **a**, the steady state developed rapidly, and the concentration remained the same after 1 ms. The steady-state values were used to draw **b**. The uniform irradiation condition does not ideally describe the experimental conditions; nonetheless, the concentrations of e_h^-, H•, and H_2 are expected to increase with increasing EDR. **c**, Parameters used for electron dose rate calculation. Screen current, beam radius, and magnification used in three different conditions and corresponding EDRs. These parameters set at the described magnification were measured in TEM user interface software and used to calculate the EDR values. Fluctuations in the screen current are shown on a percentage scale and are almost negligible.

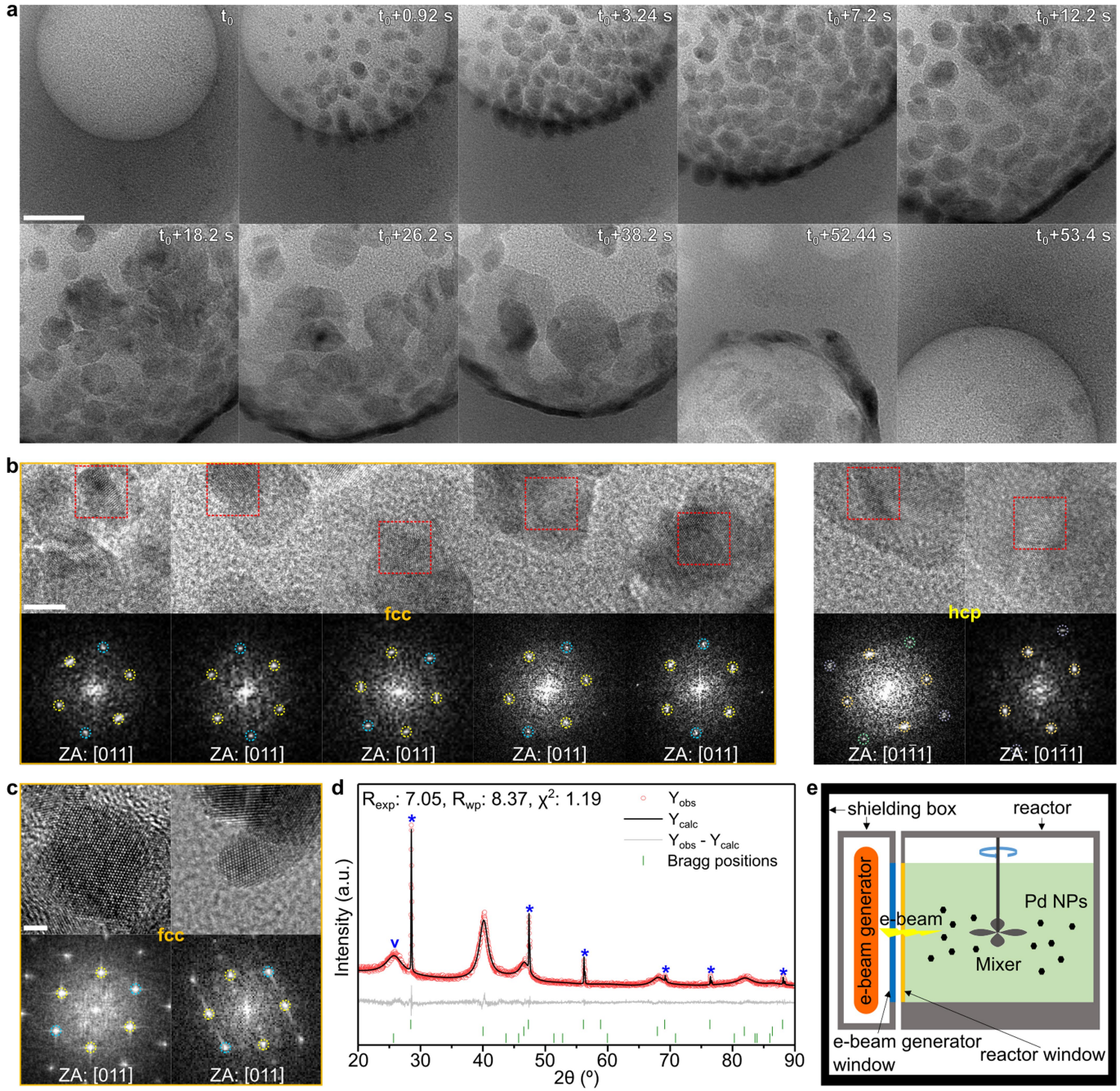

Extended Data Fig. 4 | Formation of nanoparticles around a hydrogen bubble evolved in GLC and in a batch reactor outside TEM. a, Sequence of TEM images acquired by in situ analysis, showing the nucleation and subsequent growth and dissolution of nanoparticles on the surface of a bubble, recorded under high EDR. These particles are thought to be generated via the condensation of Pd ions around a bubble as gas molecules push other chemicals away. **b**, In situ HR-TEM images and corresponding FFTs of the nanoparticles formed on the surface of the bubble in **a**. Both fcc and hcp nanoparticles were generated. Notably, the interplanar distances of the fcc particles are 3–4% larger on average than those of pure fcc Pd, indicating the formation of fcc PdH_x particles. The production of fcc particles around hydrogen bubbles (which form when the radiolysis products exceed their critical concentration[9]) is another piece of evidence for the key role of H in the formation of the hcp structure. These bubbles remove supersaturated H, resulting in a lower H/Pd condition favoring the formation of fcc PdH_x around the bubble. **c**, Ex situ HR-TEM images of Pd nanoparticles grown on the surface of carbon black in a batch reactor that utilizes an electron beam with a dose rate of 1.9×10^{-3} $e^- Å^{-2} s^{-1}$, showing only fcc particles. **d**, Le Bail fitting results for the XRD pattern of the Pd/C synthesized in the batch reactor. The asterisks and the "v" mark on the peaks correspond to internal standards of Si powder (NIST SRM 640e) and graphite (PDF# 04-006-5764), respectively. **e**, Schematic illustration of electron-beam-assisted Pd nanoparticle synthesis using a large-scale batch reactor. Scale bars, 20 nm (**a**), 5 nm (**b**), and 2 nm (**c**). ZA, zone axis.

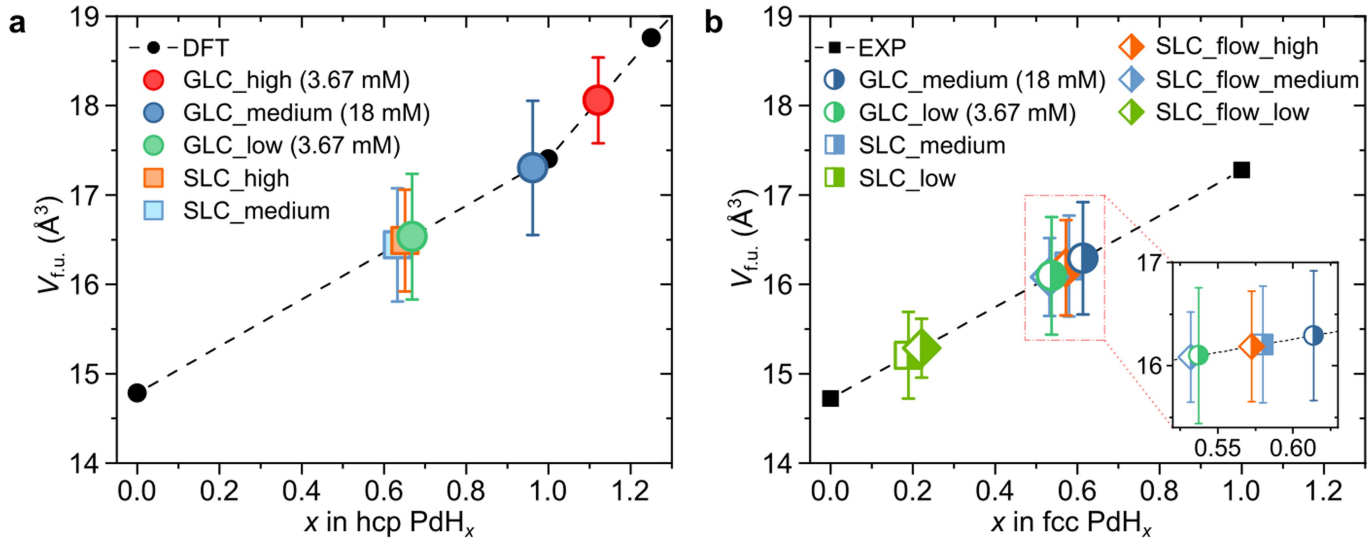

c

	GLC										SLC			
	3.67 mM		10 mM		18 mM		36.7 mM		73 mM		static		flow	
	hcp	fcc	hcp	fcc	hcp	fcc	hcp	fcc	hcp	fcc	hcp	fcc	hcp	fcc
High	29		18		27		22		32		58		38	29
Medium	67		63		40	20	18	25	47	42	17	19		29
Low	51	17	41	22	40	37	26	48	37	55		30		34

Extended Data Fig. 5 | Calculated and experimental $V_{f.u.}$ of hcp and fcc PdH$_x$. a, **b**, Comparison of $V_{f.u.}$ of the nanoparticles and bulk phase for hcp (**a**) and fcc (**b**) PdH$_x$. DFT-calculated and experimental volumes were used for bulk hcp PdH$_x$ and fcc PdH$_x$, respectively. In the DFT result, H atoms are placed at the tetrahedral sites after all the available octahedral sites are filled for x greater than 1. The H content x in the nanoparticles, which is unknown, is deduced from the volume of the corresponding structure in bulk. A linear volume change with respect to x is assumed for the interpolated x values. The $V_{f.u.}$ of both hcp and fcc nanoparticles increased with increasing EDR owing to the corresponding increase in H concentration in the solution. Error bars represent standard deviations. **c**, Total number of particles used for deriving $V_{f.u.}$.

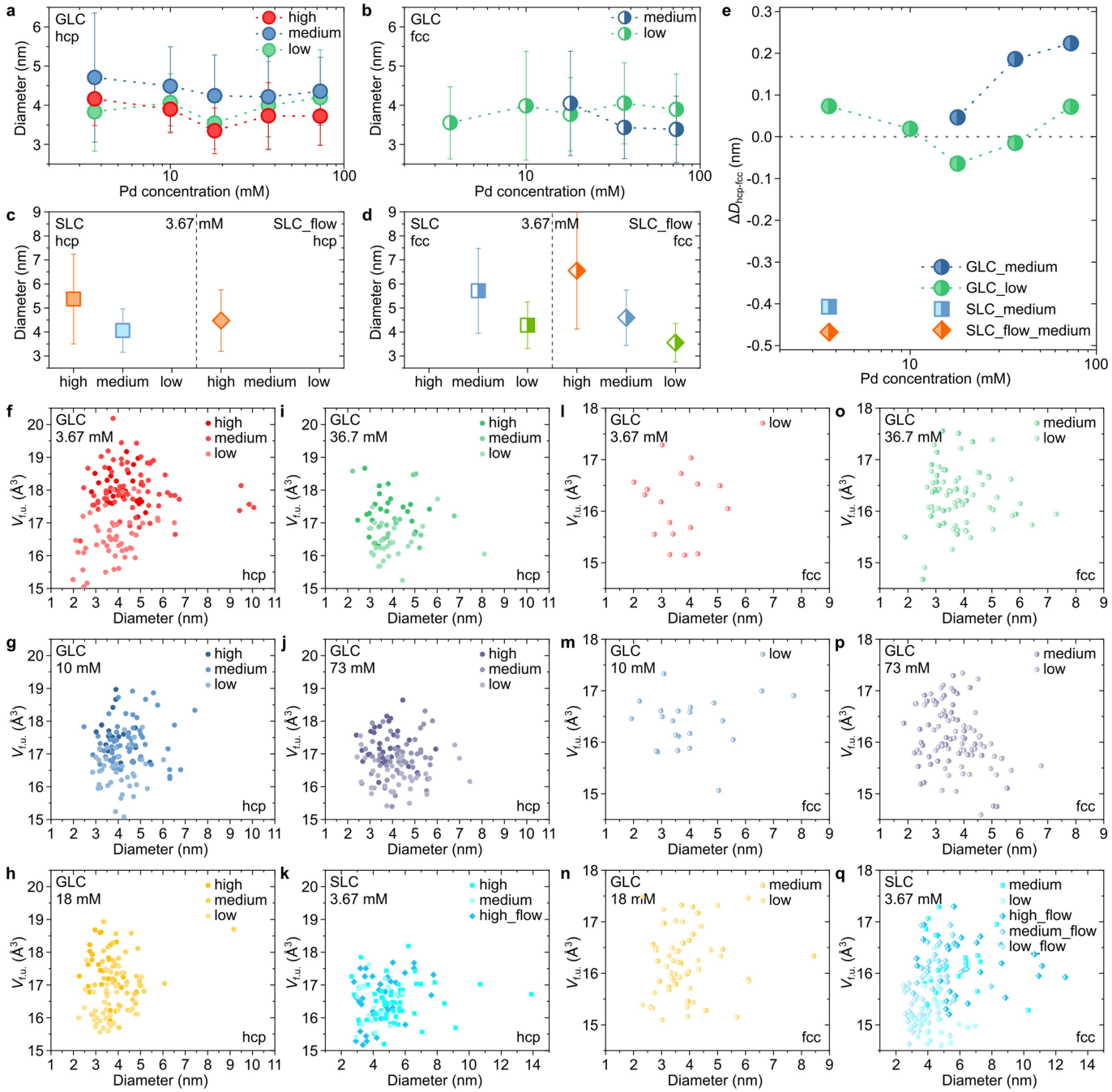

Extended Data Fig. 6 | Average size and distribution of particles. **a**, **b**, Average size of hcp (**a**) and fcc (**b**) PdH_x nanoparticles in GLC with respect to EDR and Pd concentration. **c**, **d**, Average size of hcp (**c**) and fcc (**d**) PdH_x nanoparticles in SLC in static or flow mode with respect to EDR at a fixed Pd concentration (3.67 mM). Error bars represent standard deviations. **e**, Size difference between hcp and fcc particles ($\Delta D_{hcp\text{-}fcc}$) formed in conditions where both phases were observed. The average diameter of hcp particles subtracted from that of fcc particles is plotted as a function of Pd concentration, EDR, and liquid cell system. No clear trend was observed, possibly because of the complexity of the radiolysis process. Not only the average particle size and its distribution but also the total number of particles depend strongly on both the Pd and hydrated electron concentrations. These factors, along with other radiolysis-driven conditions, including hydrogen ion/radical concentration and pH, significantly influence the nucleation and growth rate of PdH_x nanoparticles, which in turn determines the size distribution of the particles according to classical nucleation theory[59]. Furthermore, the difference in irradiation time for each EDR condition as well as the limited supply of Pd in GLC could affect the particle size and the total number of nanoparticles. Hence, it is difficult to achieve a comprehensive understanding of the size of the particles produced in the liquid cells. No systematic change was observed in the particle size of either hcp or fcc particles (**a**, **b**) or their size difference (**e**) with respect to Pd concentration and EDR. The number of datasets in the case of SLC (**c**, **d**) was not enough to find a reliable trend. **f**–**q**, Distribution of $V_{f.u.}$ and particle diameter of hcp (**f**–**k**) and fcc (**l**–**q**) PdH_x nanoparticles formed in GLC and SLC as a function of Pd solution concentration: 3.67 (**f**, **l**), 10 (**g**, **m**), 18 (**h**, **n**), 36.7 (**i**, **o**), and 73 mM (**j**, **p**) in GLC and 3.67 mM (**k**, **q**) in SLC depending on EDR. Conditions where either of hcp phase or fcc phase particles were barely observed were omitted. $V_{f.u.}$ and particle diameter show no correlation with any of the three factors, EDR, Pd concentration, and liquid flow.

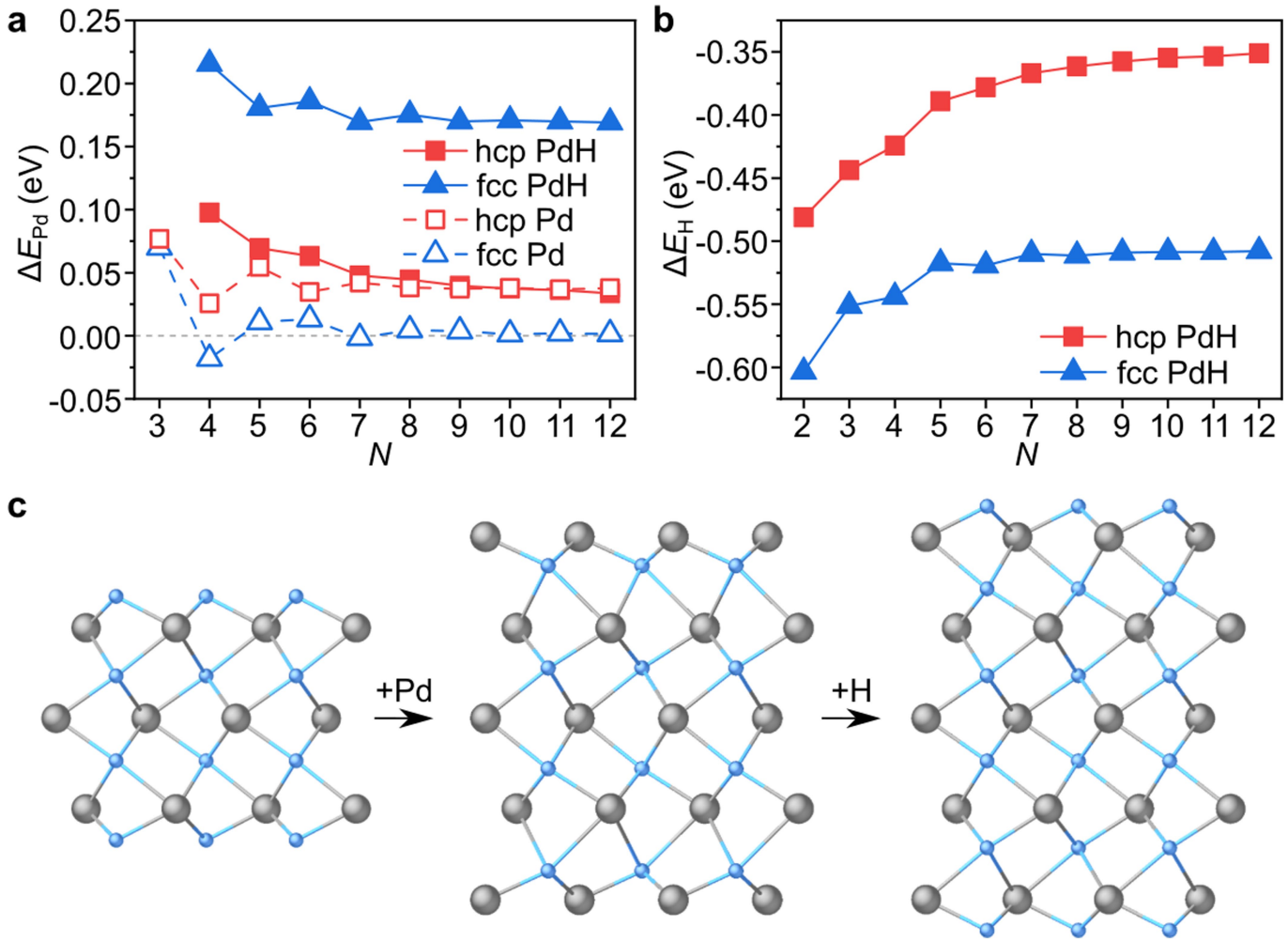

Extended Data Fig. 7 | Energy of the PdH slab growth. a, **b**, Energy required to symmetrically add Pd (**a**) or H (**b**) atomic layers on top of the (0001) hcp PdH or (111) fcc PdH slab, estimated from DFT calculations. **c**, Illustration of the symmetric addition of Pd and H layers, with Pd and H atoms drawn in gray and blue, respectively. The energies are defined as $\Delta E_{Pd}(N) = 1/2\times((E(Pd_NH_{N-1})-E(Pd_{N-2}H_{N-1})-2\times E(\text{fcc Pd}))$ for the addition of N Pd atoms in **a** and $\Delta E_H(N) = 1/2\times((E(Pd_NH_{N+1})-E(Pd_NH_{N-1})-E(H_2))$ for the addition of N H atoms in **b**. In the case of fcc and hcp Pd slabs, the energy for Pd addition is simply expressed as $\Delta E_{Pd}(N) = E(Pd_N)-E(Pd_{N-1})-E(\text{fcc Pd})$; for fcc Pd, $\Delta E_{Pd}(N)$ approaches zero, whereas for hcp Pd, it approaches the energy difference between bulk hcp Pd and fcc Pd, which indicates that convergence has been achieved. Although $\Delta E_{Pd}(N)$ for hcp PdH and hcp Pd are similar, $\Delta E_{Pd}(N)$ for fcc PdH is higher than that for fcc Pd and even than that for hcp PdH.

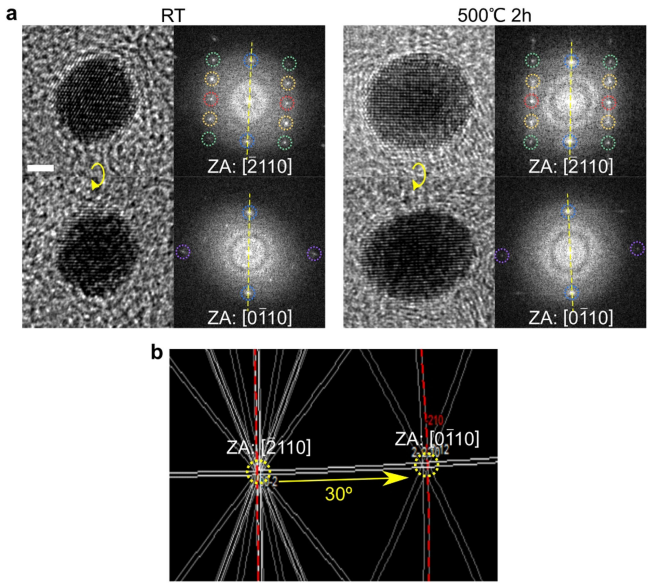

Extended Data Fig. 8 | Annealing a hcp PdH_x nanoparticle. a, Ex situ HR-TEM images and corresponding FFTs of a nanoparticle as synthesized at room temperature (RT) and after being annealed at 500 °C for 2 h. The hcp PdH_x nanoparticle maintained its crystal structure and interplanar distances even after heat treatment. Images were acquired with two different zone axes for a single particle to confirm the hcp structure. **b**, Tilting a particle initially aligned along the [\overline{2}110] axis by 30° around an axis along the [0002] direction reoriented it to alignment along the [0\overline{1}10] axis, as expected in the Kikuchi pattern of hcp with $c/a = 1.65$. Scale bar, 2 nm. ZA, zone axis.

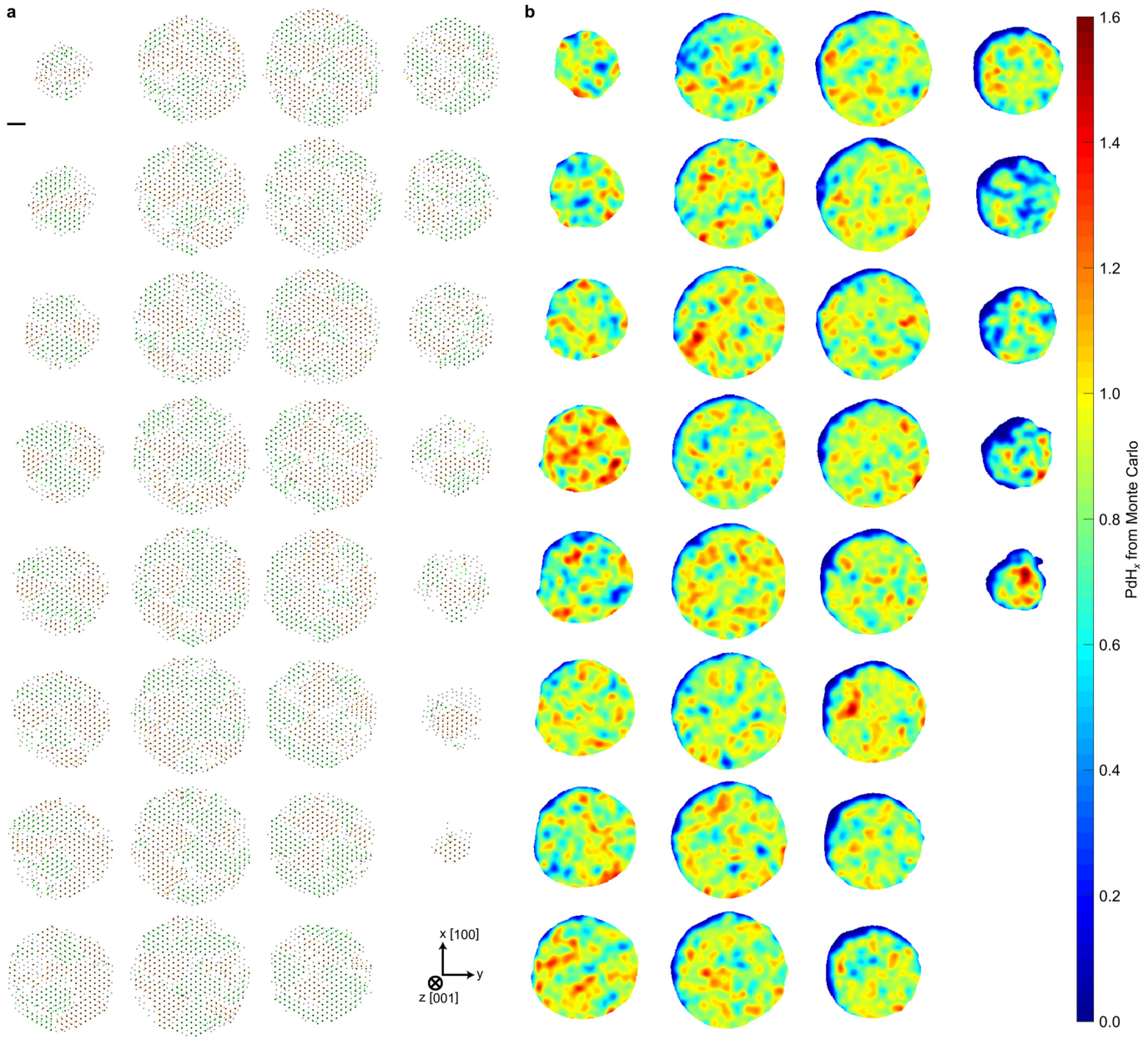

Extended Data Fig. 9 | Detailed atomic structure and local H concentration map of a PdH$_x$ nanoparticle obtained in the GLC, showing large local fluctuations. a, Layer-by-layer representation of the traced atomic coordinates and fitted hcp positions for two major domains of the PdH$_x$ nanoparticle shown in Fig. 4. The atoms belonging to two major domains are shown in orange and green. Each domain was separately fitted with a hcp structure, and black dots represent atoms fitted to the hcp positions. Gray dots represent the atomic positions not assigned to any domain. The layers were sliced from the top of the nanoparticle along the hexagonal *c* axis and plotted in vertical order starting from the top left panel. **b**, Layer-by-layer representation of the local H concentration map calculated from MC simulations using Pd coordinates constructed from the AET results, where the layers are ordered corresponding to **a**. The local fluctuation of H correlated with the large fluctuation in lattice constants (0.1–0.2 Å) observed in the statistical ex situ analysis of hcp particles (Fig. 3 and Extended Data Figs. 5a and 6f–k) as well as in situ analysis of particle growth, showing fluctuations in the *d*-spacing during particle growth (Fig. 1c–d). These local fluctuations might stem from the nonuniform H distribution in the liquid owing to the stochastic collisions of incident electrons and water molecules. A high H molar concentration appears near the Pd atoms with a large local lattice constant, where the H concentration reaches up to 150% of the Pd concentration. Approximately 20% of the total H atoms are found to occupy the surface region. The lower spatial H concentration marked at the surface region is due to the difference in accessible free volume per Pd atom, where surface Pd atoms have a larger Voronoi volume than the inner Pd atoms owing to less overlap with other Pd atoms. Scale bar, 1 nm.

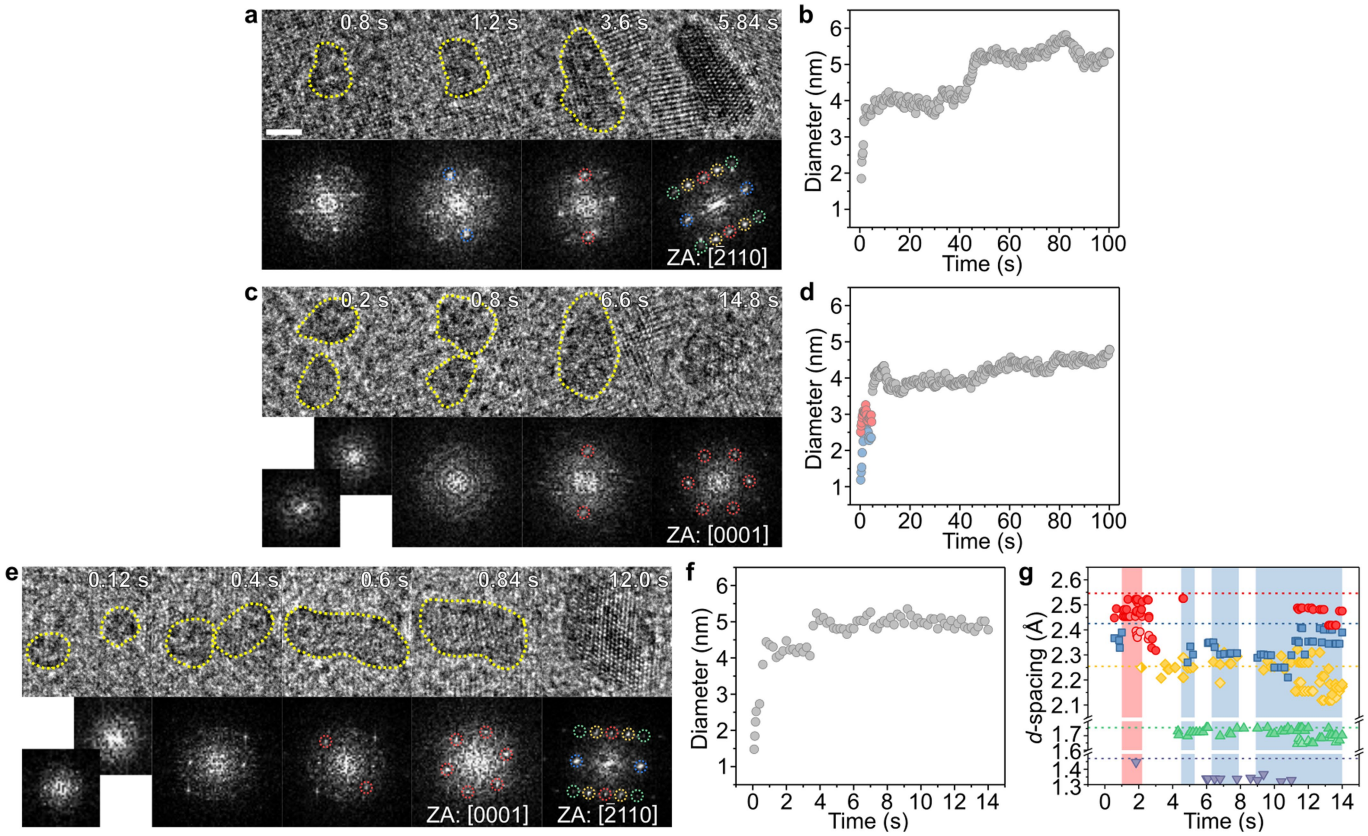

Extended Data Fig. 10 | Evolution of hcp PdH_x nanoparticles in the early growth stage and multistep crystallization process. a–**d**, Snapshots and corresponding FFTs from Supplementary Video 1 and 2 showing the early stages of the growth of particles 1 (**a**) and 2 (**c**) in Fig. 1a–d, along with **b** and **d**, their respective size evolutions. **e**, Snapshots and corresponding FFTs from Supplementary Video 4 showing the growth of another hcp PdH_x particle formed under the same conditions as those of particles 1 and 2. **f**, Size evolution of the particle in **e**. **g**, Plot of interplanar distances of five low-index planes of the particle in **e** as a function of time. The zone axis patterns show that the particle had a hcp structure immediately after coalescence, that is, within approximately one second of nucleation at most. All images were obtained in situ. Scale bar, 2 nm. ZA, zone axis.

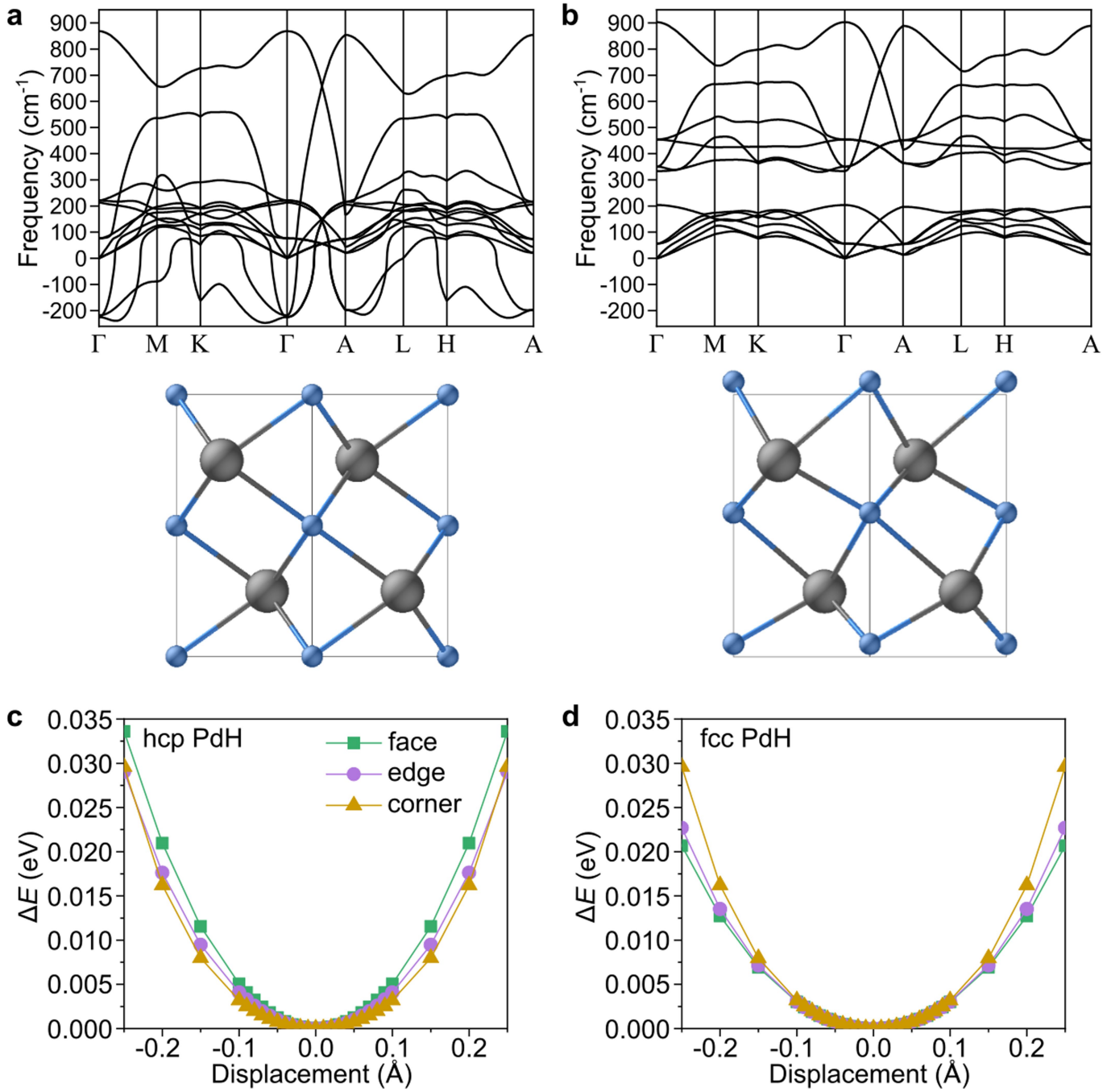

Extended Data Fig. 11 | Vibrational characteristics of PdH from DFT calculations. a, **b**, Phonon dispersion curves of hcp PdH, in which H is located at the ideal octahedral position (**a**) and H is displaced by 0.24 Å from the ideal position along the *c* axis (**b**). The corresponding atomic models are shown below the curves. Pd and H atoms are drawn in gray and blue, respectively. Imaginary phonon modes were found when H was positioned at the ideal octahedral site. One of those modes indicates the displacement of H along the *c* axis, with this rearrangement removing the imaginary modes, as shown in **b**. **c**, **d**, Energy landscape (ΔE) values around the octahedral position as calculated by displacing a single H atom from the center of the octahedron made by the six nearest-neighboring Pd atoms in the 48-atom supercell (2 × 2 × 3 hexagonal cell) of hcp PdH (**c**) and fcc PdH (**d**). The displacement toward the face in **c** is similar to the changes shown in **a** and **b**, but the instability is not captured. H atoms may adopt the ideal octahedral position at room temperature instead of collectively moving to the lower symmetry structure because of the small energy difference (~1 meV/atom) between the two structures **a** and **b**. The energy variation in fcc PdH in **d** is more isotropic and lower in magnitude for the same degree of displacement than that in hcp PdH. This result agrees with the higher phonon frequencies of hcp PdH in this study compared with those of fcc PdH[54].